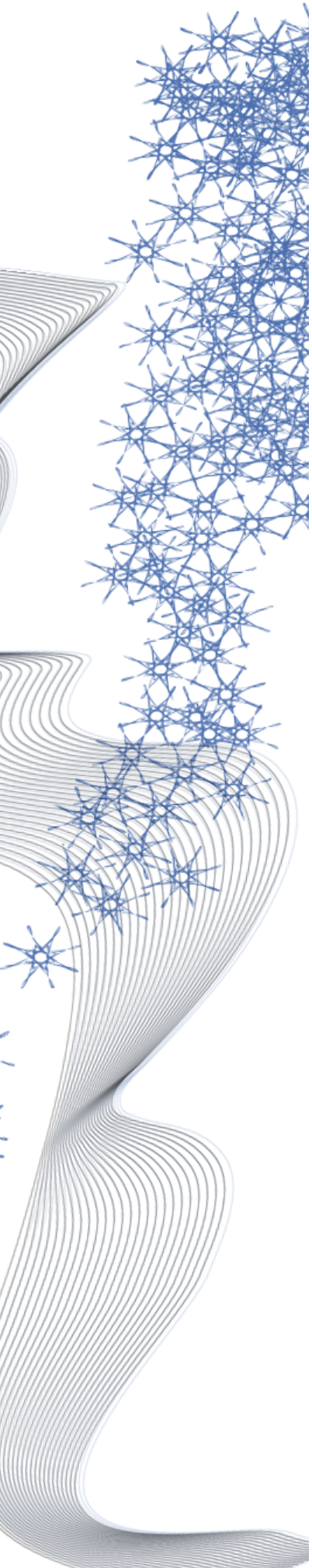

UNIVERSITY OF TWENTE.

Faculty of Science and Technology,
Advanced Technology

Optimization model describing the performance of a 3-phase coreless brushless axial flux PM machine with dual Halbach array.

Judith Tel

BSc Thesis
July 2022

Supervisors:
dr. M.M.J. Dhallé (Marc)
ir. E.L. de Weerd (Eddy)

Energy, Materials and Systems (EMS)
Faculty of Science and Technology (TNW)
University of Twente
P.O. Box 217
7500 AE Enschede
The Netherlands

Contents

1 Introduction **1**
- 1.1 Motivation and context . . . 1
- 1.2 Literature research . . . 3
- 1.3 Research question . . . 3
- 1.4 Report organization . . . 4

2 Theory **5**
- 2.1 Principles behind an electric motor . . . 5
- 2.2 The Solar Team Twente motor . . . 6
  - 2.2.1 Mechanical description . . . 6
  - 2.2.2 Mechanical losses . . . 7
  - 2.2.3 Halbach array . . . 9
  - 2.2.4 Magnetic Field analysis . . . 9
  - 2.2.5 Electrical description . . . 10
  - 2.2.6 Electrical losses . . . 11
- 2.3 Motor constants . . . 13
  - 2.3.1 Torque constant . . . 13
  - 2.3.2 Back-EMF constant . . . 14
- 2.4 Conclusion . . . 15

3 Model **16**
- 3.1 Optimization Model . . . 16
  - 3.1.1 Model workflow . . . 17
- 3.2 Design parameters . . . 17
  - 3.2.1 Overview design parameters . . . 18
- 3.3 Limits . . . 18
- 3.4 Requirements and operating conditions . . . 20
- 3.5 Motor losses and performance . . . 21
- 3.6 Conclusion . . . 22

4 Experiment **23**
- 4.1 Test setup . . . 23
- 4.2 Test procedure . . . 24
- 4.3 Conclusion . . . 25

5 Results **26**
- 5.1 Magnetic field measurement results . . . 26
- 5.2 Model results . . . 29

5.2.1 Model output . . . 30
5.2.2 Model parameters analysis . . . 30
5.3 Conclusion . . . 33

6 Discussion **34**
6.1 Model . . . 34
6.1.1 Interpretation results . . . 35
6.1.2 Model parameters analysis . . . 35
6.2 Magnetic field experiment . . . 36
6.3 Model Verification . . . 37
6.4 Alignment factor . . . 38
6.5 Conclusion . . . 39

7 Conclusion **40**

8 Acknowledgments **42**

References **43**

Appendices

Nomenclature

α_c	The temperature coefficient of copper.
$\square$	Wire misalignment factor
ℓ_x	where x can equal phases a, b or c. The entire length of a single phase wire.
η_a	Wire misalignment factor
η_c	Litz bundle compression factor, that determines the space each bundle requires inside the stator.
ω	Angular velocity of the motor
ω_e	Electric angular velocity
ω_{avg}	Average angular velocity of the system during operation, in this case during the race.
ω_{req}	Required maximum angular velocity that the motor should be able to deliver.
ϕ_B	Magnetic flux from the dual Halbach array configuration
ρ	Mass density of the fluid
σ	Conductivity, in the paper used as the conductivity of the litz wires.
τ_{motor}	Torque generated by the motor.
$\mathcal{T}_{profile}(x)$	Function that returns the required torque of the solar car during the race for a given distance
τ_{req}	Required maximum torque that the motor should be able to deliver.
θ_c	Pitch angle of the sprung mass
θ_e	Electric angle of the motor, generally used for the angle of the back-EMF
A_M	Cross sectional area of the motor
A_{wire}	The area of a wire in a single wire segment perpendicular to the magnetic field and the direction of the angular velocity
B_{peak}	Peak value of the magnetic field at the wires.
B_{pm}	The peak field strength of the permanent magnets at the surface of the Halbach array
C_{DM}	Rotational drag coefficient
c_{sf}	Damping coefficient of the suspension of the motor wheel
d_a	Air gap between magnet rings
d_i	Inner diameter magnet ring
d_o	Outer diameter magnet ring
d_s	Shim distance between rotor halves
d_{se}	Diameter of a single litz wire strand.
E_x	where x can equal phases a, b or c. The generated back-EMF voltage of each phase.
F_{motor}	Force generated by the motor.
$f_m s_{litz})$	Function that returns the mass of litz wire per meter for a given number of strands and litz strand diameter.
$f_R(s_{litz})$	Function that returns the resistance of litz wire per meter for a given number of strands and litz strand diameter.
$f_{s_{litz}}(d_{bundle})$	Function that returns the number of litz strands for a given bundle diameter and litz strand diameter.
F_x	where x can equal phases a, b or c. Force generated by a single phase in the motor.
g_r	Road surface elevation
h_w	Radial thickness magnet ring
h_{aw}	Axial thickness magnet ring
I_x	where x can equal phases a, b or c. Current through each phase to neutral, this is AC current.
I_{dc}	Current from the battery, considered a DC source.
I_{max}	Maximum peak current of the phase current send to the motor, typically limited by the motor controller, battery pack or thermal limits.
I_{peak}	Peak current of a phase, which should be equivalent for each phase.
I_{RMS}	RMS (root mean square) current of a single phase.
k	The angular wavenumber
K_τ	Torque motor constant, it determines the torque that the motor generates

	per unit of peak phase current.
L_m	Phase inductance of the motor, independent of the phase.
L_x	where x can equal phases a, b or c. Phase inductance of the drivetrain, meaning the inductors and motor.
l_{mc}	Distance of the motor wheel to the centre of mass
L_{mx}	where x can equal phases a, b or c. Phase inductance of the motor.
l_{phase}	Effective length of a single phase, independent of the phase.
M	Mutual inductance of the windings in the motor.
m_{motor}	Mass of the motor
P_{aero}	Average power loss due to aerodynamic drag
P_d	Average energy lost in the suspension damping of the motor
P_{eddy}	Eddy current losses of the motor.
P_{mech}	Mechanical power delivered by the motor.
P_{res}	Power dissipated in the resistors in the motor.
P_{se}	Eddy current losses of a single wire.
P_{weight}	Average energy lost due to the mass of the motor
R_m	Phase resistance of the motor, independent of the phase.
R_x	where x can equal phases a, b or c. Phase resistance of the drivetrain, meaning the inductors and motor.
r_i	Inside radius of the magnet ring
r_{motor}	The radius of the magnetic rings, which is the average distance from the point of rotation to the force generation.
R_{mx}	where x can equal phases a, b or c. Phase resistance of the motor.
r_o	Outside radius of the magnet ring
r_{wheel}	Radius of the wheel of the solar car.
S	Vector area surface intergral
s_{litz}	Total number of strands in the litz wire.
T_{motor}	Temperature of the windings of the stator.
t_m	Number of turns in the motor (equal to the amount of wires in each segment).
V_x	where x can equal phases a, b or c. Voltage over each phase to neutral inside the motor.
v_{car}	Velocity of the car.
V_{dc}	Voltage from the battery, considered a DC source.
V_{EMF_x}	where x can equal phases a, b or c. The entire length of a single phase wire.
V_{peak}	The peak of the voltage differences between the generated back-EMF of two phases (where the single phase voltage is defined as the voltage between the motor controller and the neutral point).
V_{system}	Voltage of the system, typically the average or minimum voltage of the battery pack.
x_a	Distance to the Halbach array, from the surface of the array on the enhanced side.
x_c	Vertical displacement of the sprung mass
x_t	Vertical displacement of the tire
x_w	Losses per added kilogram of mass.

Chapter 1

Introduction

The general goal of this research is to optimize the performance of a 3-phase coreless brushless axial flux permanent magnet machine with dual Halbach array, a specific type of electrical motor. This report describes the dedicated optimization model that was constructed to optimize the performance of a particular implementation of this motor type by changing key design parameters of the motor. In this introductory chapter I will first present the general motivation and framework for this research. Next the specific aim of this work is discussed and concrete research questions are given. Finally, a short overview of the report organization is shown.

1.1 Motivation and context

The research question originally developed when I was part of Solar Team Twente (STT), a student team that builds a solar car to join the Bridgestone World Solar Challenge (BWSC). During the challenge, teams from all around the world bring their new solar car to Australia and compete for the world championship. The team that crosses through 3000 km of Australian outback the fastest with a car that is powered only by the sun and a single battery charge wins. Every two years, a team is formed that will build a new solar car.

However, the last edition the BWSC was canceled due to COVID-19 restrictions and a new alternative race was organized: Solar Challenge Morocco. This new race was set in Morocco, where top teams from Europe drove more than 2500 kilometers in extreme conditions that put the team and car to a test. After 5 days of driving on winding roads through the foot of the Atlas mountains, Solar Team Twente crossed the finish line as the winners of Solar Challenge Morocco.

The efficiency of the solar car is key to winning, so each component is continually optimized. During the edition I was responsible for the strategy and partly also for the electrical system of the car. Although I have assisted with all electric components of the car, my main responsibility was the design of the electric motor. This Bachelor's (BSc) thesis is written based on a part of the work that I have done on optimizing the motor during the year I was part of Solar Team Twente.

Since this is not the standard way a BSc research is planned and executed, my work and contributions were evaluated in consultation with my supervisors, M. Dhallé and E. de Weerd. Together we have identified a single area of research to focus on in this report, with my supervisors helping greatly to bring focus into research that was originally conducted over a longer period of time, in parallel with other activities. The main criteria for this selection were originality and independence. This means that the work described in this report is new and adds significantly to the state of the art of motor modelling within STT. The work should also be mine, I carried out most of the modeling and experimental work by myself. An additional requirement was that this report should be 'coherent' (it forms

Figure 1.1: Solar Team Twente at the finish line of the Moroccan Solar Challenge with the solar car developed during the edition of 2021: Red Horizon. This photo is courtesy of Solar Team Twente, with credits to the photographer: Jerome Wassenaar.

a complete 'story') and that the value would be typical for the duration of a 'normal' Bsc assignment.

Overall during the past edition of the Solar Challange, my work on the motor can be described as follows. Initially I worked on understanding the motor as well as the origin of losses in the solar car during the race. Next, I made several motor designs for different likely system criteria of the new car. This was realized by making a model which compared different motor designs. To run and test the model, several experiments were performed to find the required input and to interpret the output. During the production and revision of the design, the race to Australia was canceled. The load-case of the motor changed significantly to meet the new requirements imposed by the Moroccan Solar Challenge. Specifically, the new motor design had to be changed since the new race was much more mountainous, such that a water cooling system had to be implemented to prevent the motor from overheating. During the development of the new water cooled motor, I helped with the design, modeling and testing.

My main contribution to the motor development is the formulation of an optimization model what allows the user to compare the effectiveness of different design choices. Since 2013, STT has been driving with a motor that the team developed, consisting of a in-wheel axial flux permanent magnet motor. In the 2019 edition, the system voltage was changed drastically because of a change of battery pack. As we will see in chapter 2, the system voltage is a key parameter in the performance of an electric motor, so the motor design had to be adapted accordingly. Since the change in system voltage was decided late in the project, the motor could not yet be completely optimized. In 2021 the system voltage was changed again and the push for more capacity in battery cells and developments in battery chemistry will likely result in further changes in the future battery packs for the solar car. So, developing a model that is able to optimize the motor for a certain system voltage would help the

team to select the best battery pack for the solar car and still drive with an optimal motor.

The presented optimization problem of the motor can be described as finding the optimal wire layout and the optimal distance between the magnets for the load case of the solar car during a given race. The goal of the model is not to design an entirely new motor, but optimize within the given physical dimensions. Furthermore, STT required that the model should be accurate within $0.5W$ (about 1% of the total motor losses) for a produced motor to ensure they are able to compare different system losses correctly. To realize this precision, the model should be verified with previously built motors and realistic limits of the production process.

1.2 Literature research

Looking at the current research of the specific motor layout of STT revealed that axial flux permanent magnet machines have indeed been investigated extensively, but also that the topology of STT is less common [1]. The likely reason is that this specific topology would be more expensive and therefore less suitable for mass production. Furthermore, some research into similar motors is less relevant since the layout of the wires within the motor differs [2]–[4], and this is precisely one of the main design parameters that can be changed in the STT motor and will be investigated in this research.

The original design of the STT motor was based on the Marand axial flux motor developed by CSIRO with the ”Aurora” solar team, which was specifically designed for solar cars participating in the world solar challenge in 1997 [5]. Research can be found comparing the performance of different motor typologies (with cores or radial flux) with this type (coreless and axial flux) of motor [3], [6], but the main focus is to find the influence these large topology changes have on the performance. Some papers specify design models that optimize the power density of the motor, but do not focus on optimizing the wires for losses. Also, modeling results are not always validated with experimental results obtained from actually realized and tested motors [7]–[9]. F. Sahin does describe the design of a similar axial flux machine [10], optomizing a motor design for given system requirements. However, the requirements in her thesis result in a focus on the thermal limits and power density of the motor by changing the dimensions of the motor as opposed to this reports goal of optimizing the wire layout.

So, STT required research on how the key design parameters that can readily be varied in the current motor are linked to the system limits and requirements dictated by a given Challenge or changes in important system components. From the found relations, an optimization model can be made that will help the team develop a producible design optimized for the losses specific to the solar car.

To use such a model, the magnetic field inside the motor at different air gap distances should be known. The exact relation between distance and the magnetic field was not known, therefore it had to be measured. This experiment is also included in this bachelor thesis, to illustrate the input used for the model and report on my experimental approach, execution and analysis of the results.

1.3 Research question

In the previous sections I have established that the goal of the research is to construct an optimization model for a specific axial flux motor and to apply this model to the STT motor. Furthermore, the model results will be evaluated to ensure sufficient accuracy and robustness. The main research question of this thesis is:

What is the impact of small changes in the windings configuration and the air gap on the efficiency of a 3-phase coreless brushless axial flux PM machine with dual halbach array?

To answer this question, this report will first describe the motor and find the relevant relations between the layout and losses. Next, the key design parameters and performance are defined to construct the model. The influence of these parameters is then investigated using the output of the model and their expected variance. Comparing the changes of the motor performance for selected input variables will verify if these parameters indeed completely describe the observed changes in performance. At the end of the research, there should be an increased understanding of the relation between the design parameters and the performance of the motor. Ideally, concrete recommendations can be formulated to improve the robustness of the design and to increase the efficiency of the motor.

1.4 Report organization

This report is organized as follows. In Chapter 2, the background information on electrical motor principles and the specific STT design is given. This is the information that is required to construct the model and mostly consist of the relevant relations and losses in the motor. Chapter 3 will then describe the structure and the workflow of the optimization model. Chapter 4 gives an overview of the experimental setup that was used to measure the magnetic field, while the results of this experiment as well as the model are given in the following chapter. Chapter 6 discusses these results and evaluates the model and this research. Finally, in Chapter 7, conclusions and recommendations are given.

Chapter 2

Theory

The focus of this research is a 3-phase coreless brushless axial flux permanent magnet (AFPM) machine with dual halbach array, which is the specific type of motor used by Solar Team Twente (STT) in the solar car. The goal of this chapter is to explain how this motor functions. It will start with a short general introduction to electric motors and the principles used to convert electric energy to angular kinetic energy in 3-phase brushless PM machines.

Section 2.2 will describe the design of the STT motor and the specific configuration of the different elements introduced in section 2.1. In subsection 2.2.1 the mechanical components will be described and both the mechanical and aerodynamic losses in the system are explained. In subsection 2.2.3 the arrangement of permanent magnets and the resulting magnetic field in the motor will be described. Lastly, subsection 2.2.5 will focus on the conductors, or windings, in the motor. The connections and electrical losses will be given and the production process as well as mechanical aspects are briefly explained.

Finally, section 2.3 derives the motor constants for a non-specific design of the STT motor. These constants characterize an electric motor, the first describes the correlation between voltage (or back-EMF) and speed while the second relates torque generation to current. As such, these constants are key parameters for any model describing an electric motor, such as the one that will be developed in the next chapter.

2.1 Principles behind an electric motor

Electric motors generate torque using electromagnetic interactions. In literature, most 3-phase brushless PM motor designs are discussed in terms of the interaction of two magnetic fields. The permanent magnets are attracted or repelled by the magnetic field generated by a system of coils, which are energized such that continuous motion is created. However, in this introduction we explain the motor in terms of the Lorentz force.

Charged particles moving in stationary wires placed orthogonal to the magnetic field will create an apparent force on these wires. The magnetic field is created by permanent magnets which are placed in the rotor (the rotating element of the motor). The wires are placed in the stator (the stationery element). A conceptual sketch of this principle is shown in figure 2.1a. The magnets are placed alternately, each linked north and south magnet is called a pole, which are placed in pairs to ensure a consistent alternating field directions. The wires are also connected such that continuous current can flow that stays perpendicular to the field.

As the motor rotates, the magnetic field experienced by the wires changes. This creates a changing magnetic flux through the stator windings which produces an electromotive force (EMF) in the motor,

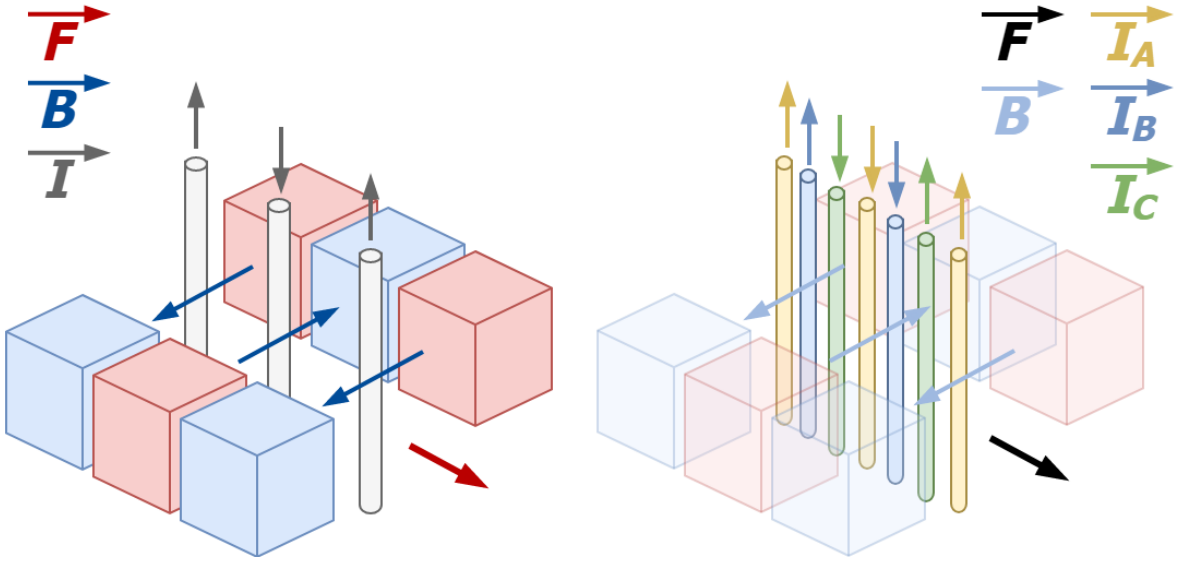

(a) Schematic overview of the force generation of conductor in an alternating electric field.

(b) Schematic overview of the 3 phase wires placed the force generation of conductor in an alternating electric field.

Figure 2.1: These figures show the basic layout the wires and magnets inside the STT motor and how this configuration translates to 3 phases.

as stated in Faraday's law of induction. The angular velocity of the motor determines the rate of change of flux and hence the amplitude and frequency of the stator EMF. We will come back to this in section 2.3.2.

The changing magnetic field will also cause a change in force at a constant current. To keep the total generated torque constant 3 different sets of wires are used, as shown in figure 2.1b. These wires each represent a phase: A, B or C, and are spaced 120 degrees from each other within a single pole. Current is sent through each phase such that the force vector from the motor is independent of the angular position. This current depends on the angle of the motor, which the motor controller can find by measuring the EMF. This measured voltage is called the back-EMF, and the frequency and magnitude are used as feedback in the motor controller to drive a 3-phase motor.

2.2 The Solar Team Twente motor

The STT motor implements the principles described above in an axial flux motor, which is sometimes called a pancake or disc motor, referring to the shape of the stator. The magnets in an axial flux motor are placed such that the direction of magnetic flux is parallel with the axis of rotation. The result is a relatively thin motor that can be designed to fit exactly inside a wheel of the solar car. The exact layout is explained in the next section, before we focus on the details of the magnets and windings.

2.2.1 Mechanical description

Figure 2.2 shows an overview of the motor with each component highlighted. The motor shaft is attached to the double wishbone suspension in the car and has the stator attached to it with bolts. Shims at the bolts ensure that the stator can be placed in the center of the two rotors. The motor shaft has two bearings which fit exactly in the left rotor half, to which the rim and wheel of the car are

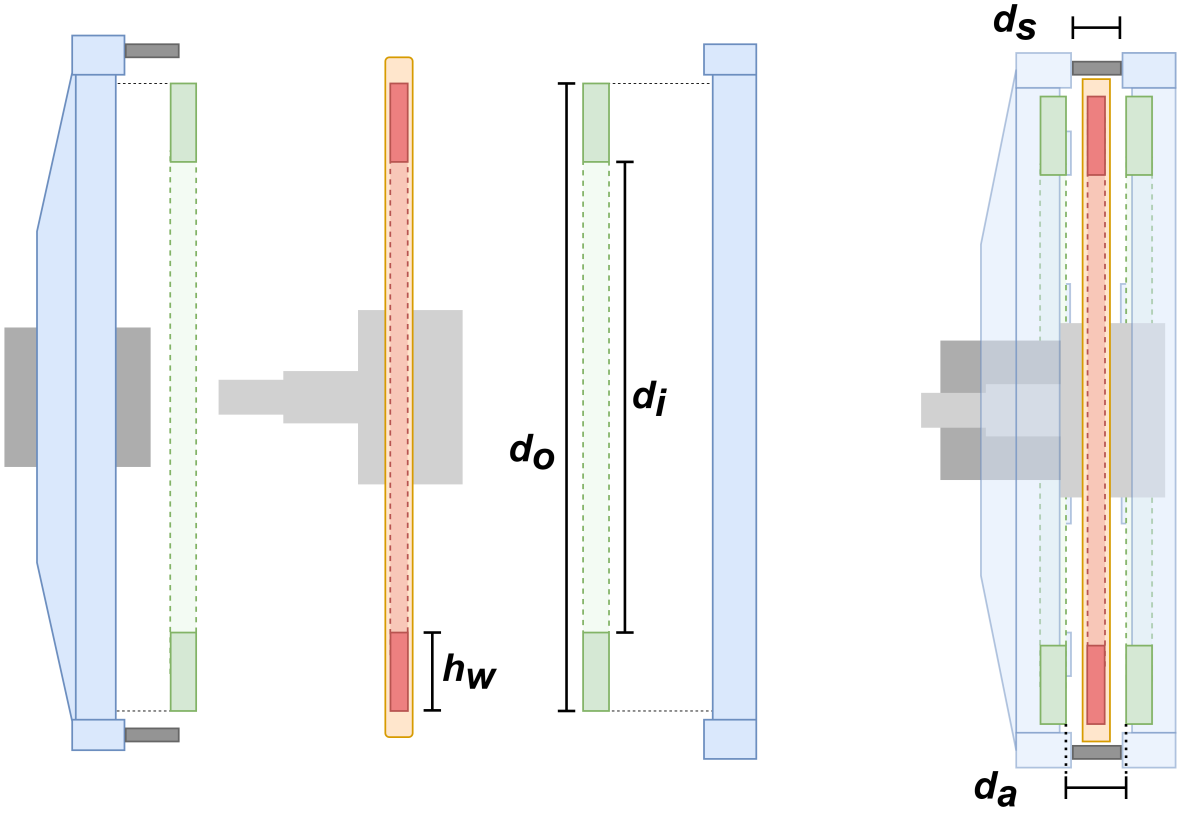

Figure 2.2: Schematic overview of the different relevant components of the motor, on the left side they are "exploded" while the right shows the assembled motor. ***Blue*** *: two rotor halves.* ***Green*** *: magnet ring.* ***Orange*** *: stator.* ***Red*** *: windings.* ***Dark grey*** *: partial thread bolts with shims.* ***Grey*** *: rotor part to fit shaft.* ***Light grey*** *: motor shaft.*

attached. The right motor half is connected to the left with a set of spacers, which are also adjustable with shims. The left motor half is called the rim rotor, while the right half is closer to the fusee and is therefore called fusee rotor.

The magnet rings are placed within the two rotor halves. The radial inner diameter of the rings is denoted by d_i and the radial outer diameter by d_o. The radial thickness is given by h_w and the axial thickness by h_{aw}. When the rings are fitted inside the structure of the rotor they should in principle protrude $1\ mm$, but the epoxy that connects the two parts can cause the rings to extend more, which may make it difficult to exactly determine the air gap. The distance between the two rings is called the air gap, given by d_a. This distance is important since the magnetic field strength depends on this distance. Furthermore, the air gap determines the maximal axial thickness of the stator, which is important for the design of the windings as will be explained in the subsection 2.2.5. The air gap is controlled by shims, which is included in figure 2.2 with the distance d_s.

2.2.2 Mechanical losses

The mechanical losses of the motor are defined as all losses caused by the movement of the motor due to friction or drag. In this optimization model the weight of the motor also needs to be taken into account as it directly influences the total efficiency of the solar car. The losses are described below and can be classified as losses from the bearings, aerodynamics and weight of the motor.

Bearing losses The bearings used in the motor are energy-efficiency bearings to reduce the driving resistance. Two bearings are placed on the shaft to reduce the axial ”play” which minimizes the camber of the wheel (the angle between the wheel and the road). This also allows for a lower air gap relative to the stator axial thickness, since the distance from stator to the magnet rings has less ”play”.

Aerodynamic losses The aerodynamic losses in the motor are determined by the turbulence of the air when driving. Since the motor housing is designed to minimize weight, gaps and thin supports are used. These gaps will cause air displacement when the motor is rotating and introduce a large air resistance. This is reduced when the motor is placed in the car, where the rim, wheel and carbon body reduce air flow to and within the motor. Nevertheless, the aerodynamic losses are a significant part of the total losses of the motor. In general, these losses can be described with the drag equation using the angular velocity:

$$P_{aero} = 0.5\rho\omega^3 C_{DM} A_M \tag{2.1}$$

P_{aero} is the average power loss due to aerodynamic drag; ρ is the mass density of the fluid, in this case air; ω the angular velocity of the motor; C_{DM} the rotational drag coefficient; and A_M the cross sectional area of the motor.

The aerodynamic losses of the motor have never been thoroughly researched by the team, but for a similar motor and housing design [11] the aerodynamic drag coefficient and reference area $C_{DM}A_M$ was found to be 0.0269e-3 m^2 using the above equation. However, these tests were performed in a test setup without wheel fairings, so the actual drag for the motor in the car will likely be lower.

Weight losses The weight of the motor has a direct influence on the total power required to drive the car at a constant velocity, which is modeled as the magnitude of the normal force times the friction coefficient of the car. Beside this loss, the weight of the motor has more influence on the total energy loss during the race as it is not supported by the suspension. This is called ”unsprung mass” and in high-performance applications it is minimized, since forward momentum is lost when tracking over imperfections in the road surface [12]. A bump in the road will transfer some momentum along the normal of the road which will cause the tire to deform and the spring damper to absorb the force, both result in losses to the system. Furthermore, a change in the normal force will introduce slippage in the motor and peak currents before the motor controller can correct for the change in grip. The most detailed analysis of the energy loss due to unsprung mass found is by C. Wei and H. Taghavifarin [13], they give:

$$P_d = c_{sf}\omega^2 0.5 \left(g_r m_{motor}(x_t - x_c + l_{mc}\theta_c)\right)^2 \tag{2.2}$$

P_d is the average energy lost in the suspension damping; c_{sf} the damping coefficient of the suspension; l_{mc} the distance of the motor to the center of mass; x_t vertical displacement of the tire; x_c vertical displacement of the sprung mass; m_{motor} is the mass of the motor; θ_c pitch angle of the sprung mass and g_r the road surface elevation. For context, the relation $g_r m_{motor}(x_t - x_c + l_{mc}\theta_c)$ represents the amplitude of the suspension’s motions. The car should be designed such that the wheel will follow the road, so the car has more grip. In this case, most energy will be lost in the damper, therefore this approximation is used.

So, the average loss of unsprung weight depends on the road surface as well as the design of the suspension. These losses have been examined by STT. The analysis falls outside the scope of this research, but I am interested in the additional loss of each added kilogram of unsprung mass. This is given by x_w W/kg.

2.2.3 Halbach array

The PM used in the STT motor have the poles shown in figure 2.1a arranged in a ring. The magnets are also placed such that they form a Halbach array, which changes the magnetic field, strengthening one side of the array while reducing it on the other side. This is done by rotating the magnets such that they follow the pattern of the preferred magnetic field on one face of the ring. This results in a stronger magnetic field near the winding. The concept is shown in figure 2.3.

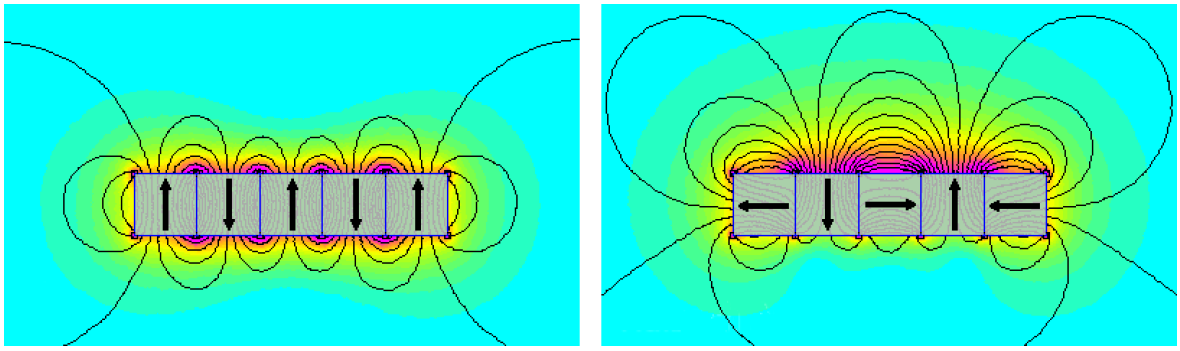

Figure 2.3: An example of a alternating magnet arrangement and a Halbach array arrangement. [14]

Depending on the specific arrangement of the magnets, the air-gap flux density will increase and harmonic distortions of the sine wave will be reduced. This effect is shown in [15], where an array with non-uniform magnet blocks is proposed that creates a more perfect sinusoidal waveform, with less harmonic distortion. Furthermore, placing two Halbach arrays opposite reinforces the field strength but maintains the sinusoidal shape of the relevant orthogonal component.

The shape of the magnetic field is important for the efficiency of the motor. As explained, the motor is controlled using a 3 phase sine wave inverter, which converts the DC voltage from the battery pack into a sine wave for each phase. The shape of the magnetic field and the wire area determine the back-EMF and therefore the voltage over the phases. Since the motor controller essentially behaves as a voltage source, the back-EMF determines in large part the current flow through the phases. The resulting current ripple on the sine wave will also generate a torque and speed ripple in the motor. When the torque ripple becomes so large it produces a counter torque, this opposing force is called the ”cogging” torque of the motor and results in ”jerkiness” and energy loss in the system. So, the harmonic distortion in the back-EMF of the motor should be reduced as much as possible. It is also possible to align the wires asymmetrically to reduce the cogging, however this will also reduce the effective current in the wires. Instead, the magnet rings in the motor are optimized to minimize the harmonics.

The specific magnet arrangement used by STT is manufactured by a partner and cannot be shared in this report. Although this layout is known by the team and the air gap can in principle be simulated, I chose to measure it experimentally. This will also give insight into the effect of non-ideal factors, such as inhomogeneity of the magnets or manufacturing tolerances. This should help increase the accuracy of the model.

2.2.4 Magnetic Field analysis

The magnetic field from a dual Halbach configuration will be described below. No array similar to the STT magnet rings could be found in literature, however, articles that use a dual Halbach configuration [16], [17] can be used to describe the magnetic field. The difference in geometry would result in different distortions and a different ratio between the dimensions of the magnet array and

magnetic field strength.

Since an ideal array forms a sinusoidal field, the relation between the air gap and the field of a single array relative to the electric angle θ_e can be described by $B_{pm}e^{-kx_a}sin(\theta_e)$. In the equation B_{pm} represents the peak field strength of the permanent magnets at the surface of the array, k represents the angular wavenumber and x_a the distance to the array. The angular wavenumber is determined by the spatial frequency of the halbach array, which is found by taking the reciprocal of distance of each spatial period. The spatial frequency is given by $n_{pp}/\left(\pi \cdot 0.5 \cdot (d_o + d_i)\right)$, which is essentially the total number of poles, n_{pp}, divided by the circumference of the magnet ring.

The two equal arrays are placed opposite each other, such that the enhanced fields are aimed towards each other and the two magnetic fields of each can be added. The distance from the array is determined to be half the total air gap d_a. Although this would be the weakest point in the magnetic field, we are only interested in the strength of the gap in the middle of the rings since the stator would be placed in the center. The equation for the magnetic field strength becomes:

$$B_{tot}(\theta_e) = B_{pm}2e^{-k\,0.5\,d_a}\ sin(\theta_e) + g_{x=d_a}(\theta_e) \tag{2.3}$$

Where $g_x(\theta_e)$ is a function of the harmonic distortions present in the field, differing per air gap distance. Simulations of halbach arrays [18] or dual arrays [15], [17] suggest the present harmonics would be dependent on the air gap, which I would expect as the interference of the two fields changes. The function $g_x(\theta_e)$ determines the torque ripple of the motor, and will be investigated in the experiments. For now it will be ignored to find the flux at a wire segment, which can simply be derived by finding the area of each wire segment.

$$\phi_B(t) = \iint_{S=A_{wire}} 2\ B_{pm}\ e^{-k\,0.5\,d_a} sin(\omega_e t)\ \ d\mathbf{A_{wire}} \tag{2.4}$$

$$\phi_B(t) = 2\ B_{pm}\ e^{-k\,0.5\,d_a} \sin(\omega_e t)\ \eta_a\ \frac{1}{2}(d_o - d_i)\ \omega_e \tag{2.5}$$

Where $\phi_B(t)$ is the changing magnetic flux; ω_e is the angular speed related to θ_e, the electric angle; S the vector area with A_{wire} being the area of a wire perpendicular to the magnetic field and the direction of the angular velocity. Since the wires could skewed, the factor η_a is added to account for this misalignment. These equations will be used in section 2.3 to derive the motor constants. The permeability of the material is ignored since air and copper are have a high relative permeability, close to vacuum.

2.2.5 Electrical description

Finally, the last element of the motor are the stator windings. This is where the current flows through and therefore determines in large part the motor characteristics. The wires inside the stator are separated into different segments, the number of segments depends on the amount of pole pairs, n_{pp}. This can be seen in the schematic overview of figure 2.1b.

As shown, each pole has 3 wire segments with a different phase. The number of turns in the stator determines the number of wires of each phase in a pole. The wires are wound such that current flows from one phase terminal to the other while the direction of the current changes in each segment of the phase. The phases are connected in a single neutral point, which is called a Wye connection of the motor. This leads to the equivalent circuit in figure 2.4 of the complete drive train.

In the figure, each phase is denoted with a, b or c, these will be generalized with x in the following paragraph. The circuit shows DC voltage and current from the battery on the left, followed by the motor controller; central in the image are the inductors for each phase, which are connected to the motor controller and the motor, shown on the right. The motor controller inverts the DC voltage V_{dc}

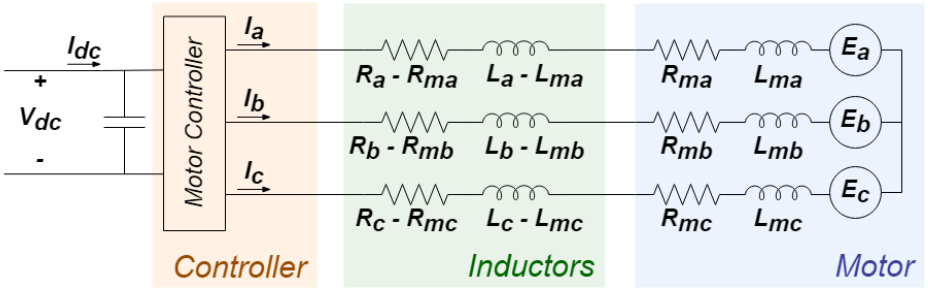

Figure 2.4: Equivalent drive train circuit with the motor controller, inductors and motor. The DC voltage and current are from a battery on the left. A similar circuit was found for the CSIRO motor [11].

and current I_{dc} from the battery to the 3-phase AC currents, given by I_x. Since the motor controller requires a certain inductance to convert the DC voltage into smooth AC phase voltages, inductors are added before the motor. The total inductance of the drive train is given by L_x, the inductance of the motor is given by L_{mx}, so the inductance of the coils would be $L_x - L_{mx}$. The resistance is similarly denoted, using R_{mx} for the motor resistance and R_x for the phase resistance. Since each phase should be equivalent, we simply use R_m and L_m to describe the resistance and inductance of a single phase in the motor in the electrical model below. Since the wires of each phase are close to each other, the motor phases will have some mutual inductance M, but this will assumed to be negligible due to the geometry of the windings. E_x represent the generated back-EMF voltage of each phase. This results in phase voltages of:

$$\begin{bmatrix} V_a \\ V_b \\ V_c \end{bmatrix} = \begin{bmatrix} R_m & 0 & 0 \\ 0 & R_m & 0 \\ 0 & 0 & R_m \end{bmatrix} \begin{bmatrix} I_a \\ I_b \\ I_c \end{bmatrix} + \frac{d}{dt} \begin{bmatrix} L_m & 0 & 0 \\ 0 & L_m & 0 \\ 0 & 0 & L_m \end{bmatrix} \begin{bmatrix} I_a \\ I_b \\ I_c \end{bmatrix} + \begin{bmatrix} E_a \\ E_b \\ E_c \end{bmatrix} \tag{2.6}$$

The wires used in the motor are copper litz wires, which are bundles of fine individually insulated strands. They are designed to carry high frequency AC signals and reduce eddy current losses. Furthermore, they are woven in a pattern by twisting the wires and groups of wires which results in an equivalent length of each strand at the outside of the conductor. This results in an equal distribution of currents among the strands which reduces resistance and ensures equivalent individual wire length when winding the bundle to produce the stator.

After the wires are wound in each segment they are compressed, which reduces the stator width. Finally they are potted (encapsulated in an epoxy resin) to protect the wires and to keep them in place. Now the stator can be placed in the rotor halves and connected to the motor controller.

2.2.6 Electrical losses

The overall losses in the electrical circuit are all losses resulting from the windings and electromagnetic interactions in the motor. Most of the electrical energy lost in the motor results in heat generation inside the stator. Since the temperature of the stator has not resulted in problems during the race, the heating of components will not be considered during the design of the motor or the calculation of electrical losses. Instead a constant motor temperature will be assumed T_{motor}.

Resistance losses The ohmic power lost in the resistance of the wires in a 3-phase motor can be calculated by finding the equivalent DC current, which is called the RMS current I_{RMS}. Assuming a perfect sine wave for each phase we find the power dissipation for a given peak current. To find the resistance of the wires during operation the temperature coefficient of the resistance is used. The final resistance loss is then given by:

$$P_{res} = \left(\frac{1}{sqrt2} I_{peak}\right)^2 \cdot 3R_m \cdot [1 + \alpha_c (T_{motor} - T_{20^\circ})] \tag{2.7}$$

Here P_{res} is the power dissipated in all resistors of the motor; I_{peak} is the peak current of a phase, which should be equivalent for each phase; α_c is the temperature coefficient of copper with a value of $4.29\text{e-}3\ K^{-1}$ [19]; and T_{20° is the reference temperature of $20 \circ C$, the motor phase resistance is determined at this temperature.

Eddy current losses The changing magnetic field induces currents in a conductor, following Faraday's law of induction. These current will form closed loops in the wires of the stator called eddy currents. Subsequently an opposing magnetic field proportional to the angular velocity of the motor will be generated. This field acts as a drag force on the motor, with the loss of kinetic energy equal to the ohmic eddy current losses.

These losses can be explicitly split into proximity losses and skin effect losses when considering inductors or individual strands [20]. The skin effect losses were analyzed for the litz wire strands used in the motor, but found to be negligible for the given motor controller switching frequency. So, the eddy current losses are considered to be equal to the proximity losses.

Papers [21] and [22] find that the losses in a single circular strand experiencing a sinusoidal magnetic field are given by equation 2.8. Considering the relevant eddy current losses to be close and perpendicular to the magnet rings the total losses for the motor at a given velocity in m/s.

$$P_{se} = \frac{\pi}{128} \sigma \omega_e^2 B_{peak}^2 d_{se}^4 \tag{2.8}$$

$$P_{eddy}(v_{car}) = \frac{\pi}{128} \sigma \left(\frac{1}{r_{wheel}} v_{car} \cdot n_{pp}\right)^2 B_{peak}^2 d_{se}^4 \cdot 3h_w \cdot 2n_{pp} \cdot t_m \cdot s_{litz} \tag{2.9}$$

Here P_{se} are the eddy current losses of a single wire, while P_{eddy} are the total eddy current losses in the motor. The litz wire strands bundles in the motor are described by: d_{se} the diameter of a single litz wire strand; s_{litz} the total number of strands in the litz wire; t_m the number of turns in the motor (equal to the amount of wires in each segment); and σ the conductivity of the litz wires. B_{peak} equals the peak value of the magnetic field at the wires; r_{wheel} the wheel radius of the solar car wheel and v_{car} is the velocity of the car.

The eddy currents in the motor have never been analyzed thoroughly by STT, however an experiment performed by the team in 2017 can be used to compare the model with experimental values. The data from the experiment and the model are shown in figure 2.5. The power losses calculated with equation 2.9 are close to the measured value, although about 20% higher. This difference can be explained by inaccurate measurements or incorrect input variables, which I think is the case. So, this model likely not exact but within the correct general range and I consider it reliable and sufficiently accurate given the research.

Hysteresis losses Since the wires of the motor form an inductor, the change in current flowing through them results in a changing magnetization of the core. This core is the epoxy between the stator windings and is mixed with small metal particles, which increase the thermal conductance of the epoxy but are engineered to maintain a high breakdown voltage. When the core is demagnetized, some remanence remains and is not converted to electrical energy. However, these hysteresis losses are also considered insignificant, as the epoxy does not have a high percentage of metal particles and the ratio epoxy to wires is low.

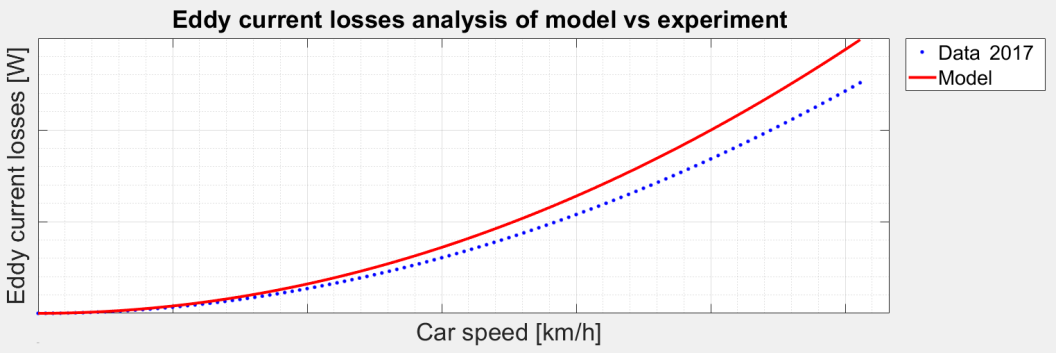

Figure 2.5: Comparison eddy loss data from a 2017 experiment of Solar Team Twente, data courtesy of STT.

2.3 Motor constants

The motor constants are used to describe the key characteristics of any electric motor and consist of the torque constant K_τ and the back-EMF constant K_E. The torque generation and speed of the motor are determined by these constants, so they are crucial when optimizing the motor.

When reviewing current research in 3-phase coreless brushless axial flux PM machines with an Halbach array, only a solution of the constants for a given magnetic flux is available for this motor that would describe the specific magnetic field and windings [10], [23]. The STT documentation of the initial motor design is incomplete and the motor constants are determined by measuring the magnetic flux. So, the motor constants were derived again with more specific inputs that contribute to the motor design. The results shown in this section were discussed and verified with Tecnotion, an expert in direct motor technology and a partner of STT.

2.3.1 Torque constant

The torque constant determines the torque that the motor generates per unit current. Since a 3-phase design is used, the unit chosen is the peak current of a single phase, which results in $K_\tau = \tau_{motor}/I_{peak}$. The value of K_τ has a strong relation to the efficiency of the motor because of the contribution to the resistance losses. This can easily be understood when comparing the mechanical power $P_{mech} = \tau_{motor} \cdot \omega$ with the ohmic power loss $P_{res} = I_{RMS}^2 \cdot 3R_m$. A higher K_τ value will result in a lower ratio of P_{res}/P_{mech}, so in a higher efficiency.

To find the constant K_τ we start with the Lorentz force for a single wire and use the previously found values assuming a perfect sinusoidal magnetic field and sinusoidal current. The motor is ”synchronous”, which means that the magnetic field should be in phase with the current for optimal force to current production. Furthermore, each phase has an offset of $120°$ and the total force the motor generates can be found by adding the forces generated by all phases. Lastly, it is important to note that this calculation is only valid using the wye connection.

$$F_x(t) = B_{peak} \cdot sin(\omega_e t) \cdot I_{peak} \cdot sin(\omega_e t) \cdot \int_0^{\ell_x} \mathrm{d}\boldsymbol{\ell} \tag{2.10}$$

$$F_{motor}(t) = F_{x=a}(t) + F_{x=b}(t) + F_{x=c}(t) \tag{2.11}$$

$$F_{motor}(t) = B_{peak} \cdot I_{peak} \cdot \left(sin(\omega_e t)^2 + sin(\omega_e t + \tfrac{2}{3}\pi)^2 + sin(\omega_e t - \tfrac{2}{3}\pi)^2\right) \cdot \int_0^{\ell_x} \mathrm{d}\boldsymbol{\ell} \tag{2.12}$$

$$\tau_{motor} = F_{motor} \cdot r_{motor} = 1.5 \cdot B_{peak} \cdot I_{peak} \cdot r_{motor} \cdot \int_0^{\ell_x} \mathrm{d}\boldsymbol{\ell} \tag{2.13}$$

$$K_\tau = \frac{\tau_{motor}}{I_{peak}} = 1.5 \cdot B_{peak} \cdot r_{motor} \cdot l_{phase} \tag{2.14}$$

Thus we find K_τ dependent on the geometry of the motor and the strength of the magnet field. Here F_x is the force generated by a phase and F_{motor} the total force generated by the motor. The torque generated by the motor is given by τ_{motor}, with r_{motor} the radius of the magnetic rings, which is the average distance from the point of rotation to the force generation.

The effective length of a single phase is given by l_{phase}. This length is the summation of all wire segments, $\mathrm{d}\boldsymbol{\ell}$, orthogonal to the field and force directions that contributes to the torque generation over the entire length of the phase wire, given by ℓ_x. The effective length of the wires depends on the number of pole pairs n_{pp}, radial width of the Halbach array h_w and the number of turns t_m, as well as an alignment factor η_a that corrects for the non-orthogonal wire segments. With these additional input factors the torque constants becomes:

$$K_\tau = 1.5 \cdot \ 2\, B_{pm}\, e^{-k\, 0.5\, d_a} \cdot \tfrac{1}{2}\left(d_i + d_o\right) \cdot \eta_a \left(2 \cdot n_{pp} \cdot h_w \cdot t_m\right) \tag{2.15}$$

In this equation the peak field strength B_{peak} has also been substituted with the amplitude of the field strength described in equation 2.5. This gives $B_{peak} = 2\, B_{pm}\, e^{-k\, 0.5\, d_a}$. So, we find that K_τ depends more specifically on the air gap d_a, on permanent magnet strength of the Halbach array B_{pm} and the effective wire length l_{phase}, expanded above.

2.3.2 Back-EMF constant

The back-EMF constant K_E, also called the velocity constant, describes the relation between the velocity of the motor and the voltage over the phases. This constant is crucial since it determines the maximum speed of the car for a given system voltage. The motor controller alone cannot boost the voltage past the DC voltage of the battery, so the motor must be designed such that the required speed can be achieved. Again we will assume a perfect sinusoidal magnetic field and derive K_E for the angular velocity of the motor ω, which is not the same as ω_e, the electrical angular velocity. First the back-EMF of a single phase V_{EMF_x} can be found from Faraday's law of induction, with $\mathbf{B}$ describing the magnetic field:

$$V_{EMF_x} = -\frac{d}{dt} \iint_{S=A_{wire}} \mathbf{B} \cdot \ d\mathbf{A_{wire}} \tag{2.16}$$

$$V_{EMF_x} = -B_{peak} \cdot \frac{d}{dt} sin(\omega_e t) \cdot \frac{d}{dt} x \cdot l_{phase} \tag{2.17}$$

$$V_{EMF_x} = -B_{peak} \cdot cos(\omega_e t) \cdot \omega \cdot r_{motor} \cdot l_{phase} \tag{2.18}$$

Note that in a wye configuration the limiting voltage determining the maximum velocity is not the peak voltage of the controller with respect to the neutral point but rather the peak of the voltage *difference* between the back-EMF of two phases. This voltage will be called V_{peak}. To find the voltage

required to control the motor, the limiting voltage, the absolute peak of the voltage difference between the back-EMF of two phases must be found V_{peak}. In this derivation I will ignore the voltage drop over the resistors present in the drive train as this is not relevant for the back-EMF constant K_E.

$$V_{peak} = \max\left[V_{EMF_A} - V_{EMF_B}\right] \tag{2.19}$$

$$V_{peak} = \max\left[B_{peak} \cdot cos(\omega_e t) \cdot \omega \cdot r_{motor} \cdot l_{phase} - B_{peak} \cdot cos(\omega_e t + \tfrac{2}{3}\pi) \cdot \omega \cdot r_{motor} \cdot l_{phase}\right] \tag{2.20}$$

$$V_{peak} = \max\left[B_{peak} \cdot \omega \cdot r_{motor} \cdot l_{phase}\sqrt{3} \cdot sin(\omega t - \tfrac{1}{3}\pi)\right] \tag{2.21}$$

$$K_E = \frac{V_{peak}}{\omega} = B_{peak} \cdot r_{motor} \cdot l_{phase}\sqrt{3} \tag{2.22}$$

Using the previously defined B_{peak}, l_{phase} and r_{motor} it is possible to find the additional input factors for the back-EMF constant. Equation 2.22 also shows the similarities between K_E and K_τ, so a relation between the two factors can be determined.

$$K_E = \sqrt{3} \cdot\ 2\, B_{pm}\, e^{-k\, 0.5\, d_a} \cdot \tfrac{1}{2}\left(r_i + r_o\right) \cdot \eta_a \left(2 \cdot n_{pp} \cdot h_w \cdot t_m\right) \tag{2.23}$$

$$K_E = \frac{\sqrt{3}}{1.5} K_\tau = \frac{2}{\sqrt{3}} K_\tau \tag{2.24}$$

2.4 Conclusion

In this chapter the physical layout of the STT motor was described, with special focus on the PM Halbach array and the stator windings. These descriptions were used to give insight into the various loss sources of the motor and to determine the torque and back-EMF constants. In the next chapter, the optimization model will use the different relations found in this chapter to estimate the impact of various design parameters on the motor's performance and thus be able to optimize the design.

Chapter 3

Model

With the theoretical basis established in the previous chapter, this chapter will introduce the model that was created to help design an efficient motor. First the general structure and work flow of the optimization model are explained in section 3.1, before the different parameters and steps in the process are discussed in more detail. Section 3.2 focuses on defining the design parameters that will be investigated, while in 3.3 the limits within the design parameters can be varied are explained. The requirements that every motor design has to meet are introduced in section 3.4. Finally, the motor performance is formulated in terms of a cost function in section 3.5 and a typical example of the models output is given as an illustration. Note that the model in principle can also be used for a different motor design in a system, but several elements although the current implementation of certain elements are specific to the design of the STT motor.

3.1 Optimization Model

The basic function of the model is to evaluate different motor designs and to determine which one has the least losses. To do this the model will construct a set of data, for which the layout of an ideal litz wire bundle for the windings is determined. Next the model filters the results for given requirements and returns the best motor design.

The parameters used in the model and the data flow are schematically represented in figure 3.1. The output also includes information regarding the expected losses and the motor constants. The main inputs of this model are the system specific values, which are the system voltage, maximum current and estimated average velocity during the race. The input B_{pm} describes the possible different magnet strength options of the PM Halbach arrays available to STT. The data connected to the model that is not considered an input and will stay constant for different systems but is required to run the model. As such, they are treated as data inherent to the model, but can be changed whenever a different motor design is used, better products to produce the motor are found or when new requirements are formulated.

The model was made in matlab. Initially all required variables are defined, next a table is used to save all the data. This table is filled with different design parameters and the calculated losses. The data saved before it is filtered and last a bar chart is made with the most optimal motor designs. The typical run time of the model is 2 minutes, when testing about 1800 different motor designs and different litz wire bundle sizes.

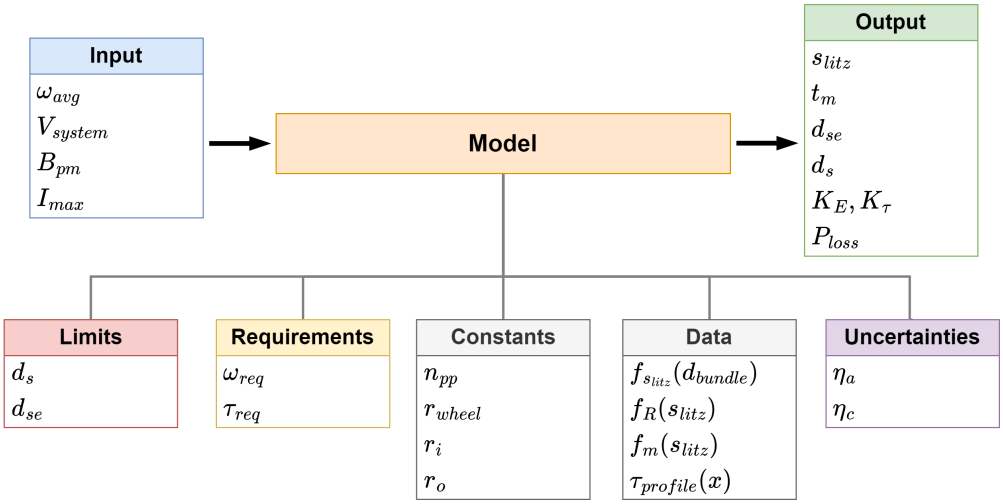

Figure 3.1: This figure shows the data used in the model as well as the data flow. For an overview of the symbols and their meaning, the reader should refer to the nomenclature at the start of this report. The input of the model is system dependent and more likely to change when a new motor design is required. The different data groups connected to the motor are considered constant when using the model. The data is grouped into Limits, Requirements Constants, Uncertainties and Data. These groups will be explained in sections 3.2, 3.3 and 3.4.

3.1.1 Model workflow

The different steps executed in the implementation of the model are explained in this section. First the model uses the input data to construct several test motor designs with the variables that determine the motor constants, as discussed in section 2.3. For a given motor constant and litz wire strand diameter, the optimal number of strands s_{litz} is calculated separately. The distance between the magnets d_a and the amount of turns determine the maximum diameter of the litz bundle. So, the max d_{bundle} and d_{se} will results in a given maximum number of litz strands. The ideal number of litz wire strands should be when $-dP_{res}/ds_{litz} = (dP_{eddy} + dP_{weight})\ /ds_{litz}$, in other words when the total loss $P_{loss} = P_{res} + P_{eddy} + P_{weight}$ as a function of the considered parameter (in this case s_{litz}) has a minimum. This principle in illustrated with example inputs in figure 3.2, where the P_{loss} was determined for different s_{litz} values.

The result of this litz wire optimization is a set of different motor designs with litz wire specifications that result in the lowest losses for the given input parameters. The next step is to filter out the motor designs that do not meet the requirements. This is done by finding the motor constant boundaries, as given in section3.4, and invalidating all motor designs whose K_E falls outside the given range. From the remaining designs the motor with the lowest P_{loss} can now be selected. An example of a typical model output is shown at the end of the chapter, in figure 3.5.

3.2 Design parameters

The design parameters are defined in this research as the parameters that influence the characteristics of the motor and that may be changed without modifying the main mechanical components of the motor. In other words, the goal is to optimize the present design, not to redesign an ideal motor. Specifically, the motor diameter as well as the magnet rings geometry are considered fixed. The permanent magnet's strength can be altered, but the number of pole pairs also remains fixed.

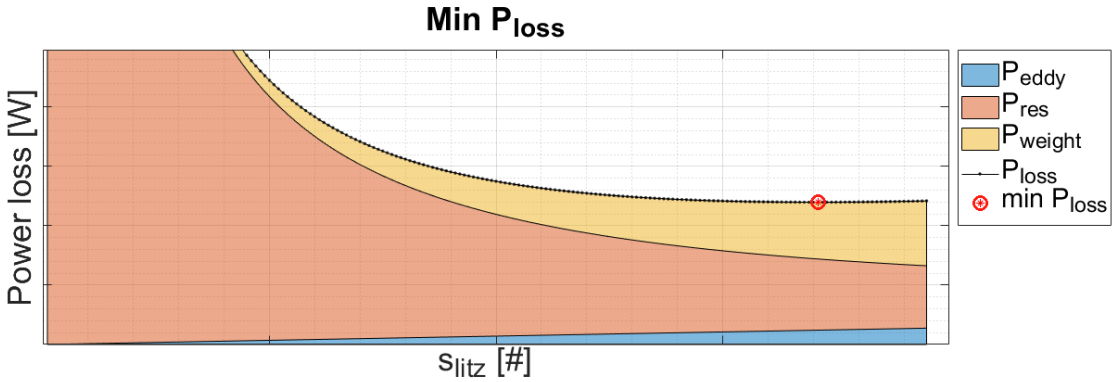

Figure 3.2: Optimization of s_{litz} for the test motor design with values given in the title.

As discussed in section 2.3, the performance of the motor is in large part characterized by the motor constants K_E and K_τ. The design parameters determining these constants can quickly be identified from equations 2.15 and 2.23. The magnetic field strength can be changed by altering B_{pm} and d_a. The air gap d_a is related to the shimm distance by $d_a = d_s + 6\text{e-}3$. Last, it is also possible to change the turns of the wires in the motor t_m.

The layout of the wires also influences the losses in the motor, as shown in equations 2.7 and 2.9. Additionally, the wires determine the weight of the motor to a large extend, as the added copper is the main difference in stator mass, and therefore the total unsprung mass of the motor. The characteristics of the wires are mainly described by the diameter and number of individual strands. The weight, resistance and diameter of the wires were fitted from the manufacturers data and are shown in figure 3.3. These data fits are used as data for the model, to automatically vary the wire characteristics in each motor design.

3.2.1 Overview design parameters

The design parameters discussed in the sections above are presented in the table below. They are the parameters considered in this research, their impact on the motor characteristics will be determined and used to optimize the motor performance. In the next section the range within which these parameters can be varied will be discussed, the relevant limits are already shown below.

Table 3.1: Overview design parameters

Parameter	***Unit***	***Limit***	***Description***
B_{pm}	T	grade a, b, c	Permanent magnet maximum field strength at $d_a = 0$
d_s	m	-	Magnet rings shimm distance
t_m		-	Number of turns of the wires in the motor
s_{litz}		-	Number of litz wire strands
d_{se}	m	-	Diameter of individual litz wires

3.3 Limits

The design parameters of the stator are constrained on one hand by the available materials and on the other hand by their implementation in the car. These limits will restrict the number of motor designs that can be tested in the model. Below the different limits are explained.

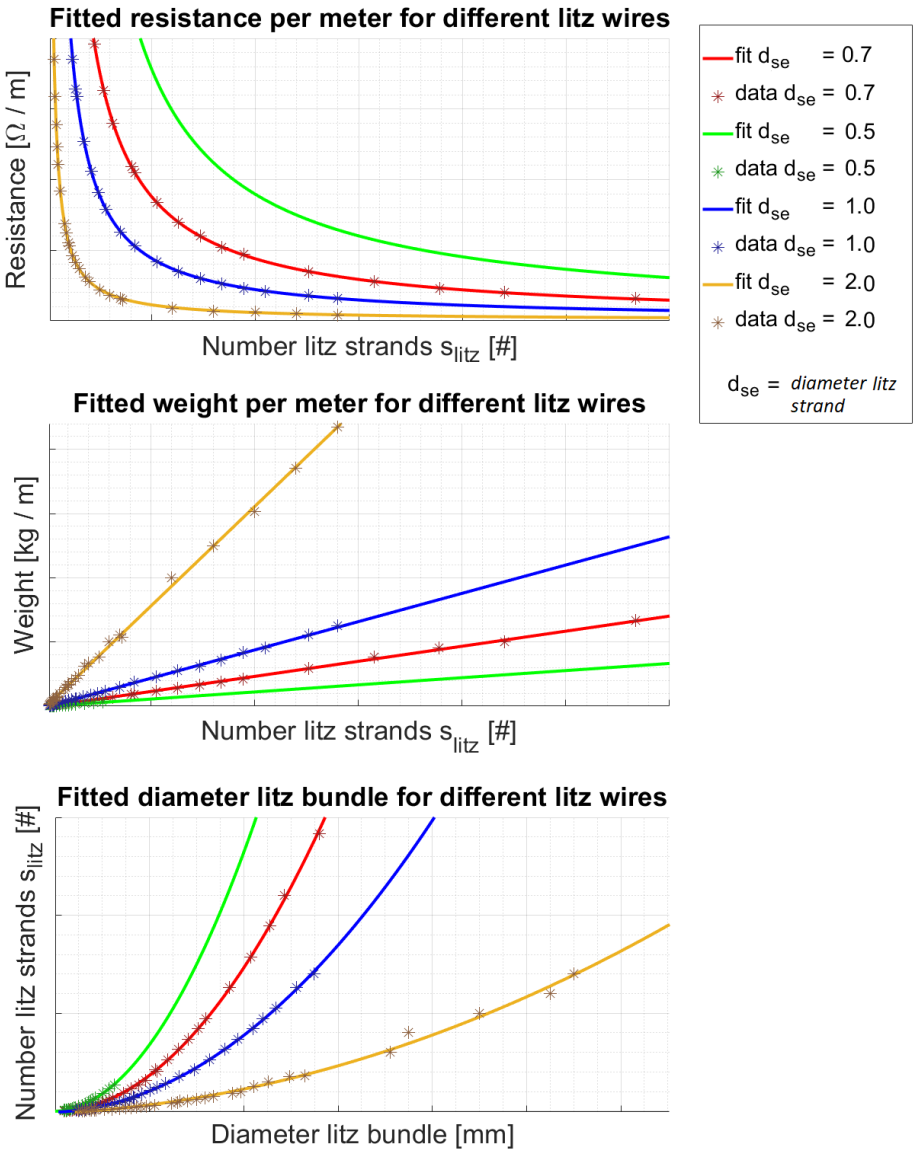

Figure 3.3: The influence of the number of strands in the stator litz wire s_{litz} and their diameter d_{se} on weight, resistance and overall diameter of the litz wires. The symbols represent the measured data published by the manufacturer [24]. The solid lines are the polynomial (for resistance and diameter) and power (for weight) fits to this data, which are used in the model calculations. The graphs have been zoomed to show the relevant range, so not all data might be visible.

The first clear limit is the fact that the motor needs to fit inside the wheel rim and suspension, which is made such that the distance between the two rotor halves, d_s, cannot exceed a set distance.

The distance d_s in turn imposes a limit on s_{litz} and d_{se}. The space between the magnet rings limits the stator thickness and therefore also the area available in each segment for the overall litz wires cross-section. The relation between the litz wire bundle diameter d_{bundle} and shimm distance d_s is as follows (with all constants and variables expressed in m):

$$A_{bundle} = \eta_c \cdot \tfrac{1}{t_m} \left(d_s + 6\text{e-}3 - 4\text{e-}3\right) \cdot \sqrt{2r_i^2 - 2r_i^2 \cdot cos\left(\tfrac{2\pi}{2 \cdot 3 \cdot n_{pp}}\right)} \tag{3.1}$$

$$d_{bundle} = 2\sqrt{\tfrac{1}{\pi}\tfrac{\eta_c}{t_m}\left(d_s + 2\text{e-}3\right) \cdot 6.295\text{e-}3} \tag{3.2}$$

The inside radius determines the width of each segment and the total stator thickness is limited by the play in the bearings as well as the basalt sheets that are added to protect the wires, resulting in $4mm$ slack. The factor η_c represents the additional space required by the wires as they are not completely compressible. This factor was found to be around □□ based on the previous stator production results. This limit will be implemented in the model when determining the optimal wire configuration.

Two additional limits are the permanent magnet strength and wire diameter. There are no permanent magnets available stronger than grade a that would not demagnetize at the ambient temperature during the race. Similarly, the diameter of the individual litz strands is limited by the manufacturer, however there are no restrictions on the number of strands.

These limits are also shown in table 3.1. The factors η_c, compression of wires, and η_a, alignment of wires, are not added in this table as they are not considered motor parameters nor limits. Instead, they are added to the model as uncertainties and give margins to possible motor designs to ensure it can be realized.

3.4 Requirements and operating conditions

Knowledge of typical operating conditions is required to find a representative load case of the motor and therefore typical losses in the system. STT uses a model of the car that can determine the torque that the motor should deliver at any given race distance, for a set speed. Since the solar cars cruise at a constant speed with minimal changes during the race, this gives a realistic torque profile. This torque profile is denoted by $\tau_r(x)$. The required torque can be seen in 3.4 and shows large deviations from the absolute mean value. This profile together with the torque constant K_τ, determine the motor current at each moment of the race $I_r(x)$. This current is used in the model to find the resistance losses.

The requirements of the motor consist of the system voltage v_{system} as well as the maximum angular velocity ω_{max} and torque τ_{max}. The system voltage is determined by the battery voltage and is considered to be a fixed input of the model, since the motor should be optimized for a given storage system. The minimum required speed is set at $105[km/h]$ to allow for quick overtaking of other teams during the race, which gives $\omega_{max} = v_{kmph} / \left(3.6 \, / \, r_{wheel}\right)$. The combination of this speed and voltage result in a limit for the value of the back-EMF constant, $K_E \leq V_{sys}/\omega_{max}$.

The required torque is determined by the regulations of the BWSC [25], which states: *"2.23.1 The fully laden solar car must be able to start from rest on a 7% gradient"*. Starting from a stationary position of the motor means that the motor controller cannot optimally drive the motor and that some energy is lost because of non-ideal current flow. To ensure the car will always comply with the regulatory requirements, a safe margin is taken. This results in $\tau_{7\%} = 1.25 \cdot sin\left(\tfrac{\pi}{45}\right) m_{car} \cdot g =$

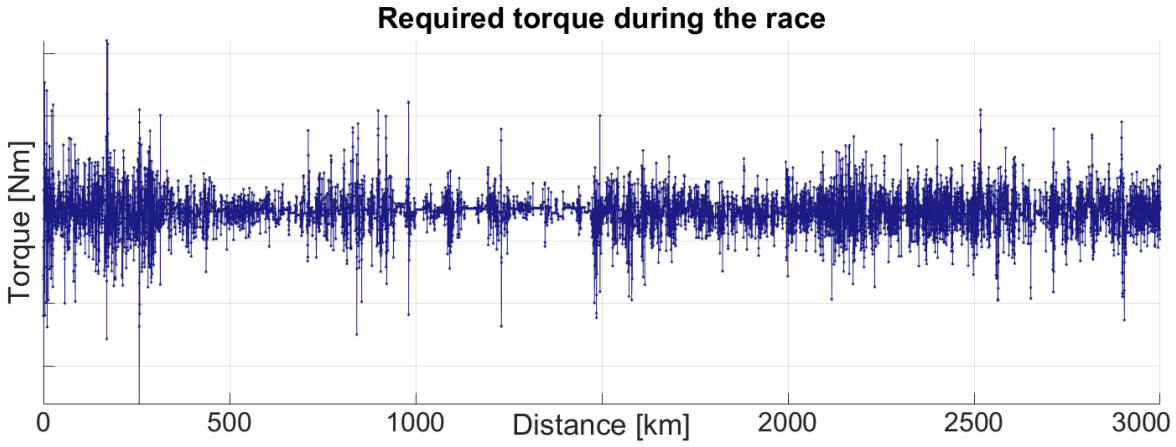

Figure 3.4: The expected torque profile of the solar car during the BWSC. This is the total torque the motor has to deliver for a predetermined velocity and was determined by a model courtesy of Solar Team Twente.

$\square\square\square[Nm]$. As can be seen by comparison with 3.4, this starting torque is much larger than the typical torque required during cruising at constant speed. The maximum peak current the motor controller can supply is given by I_{max} and depends on the design of the controller, so this limits the torque constant $K_\tau \geq \square\square\square/I_{max}$. Since the torque and back-EMF constant are related, this results in the available range of

$$\frac{2 \cdot \mathcal{T}_{7\%}}{\sqrt{3} I_{max}} \leq K_E \leq \frac{V_{system}}{\omega_{max}} \tag{3.3}$$

3.5 Motor losses and performance

The motor efficiency is generally defined as the total required electrical energy for a given kinetic energy output, tested at different velocities and torque loads. However, the goal is to minimize the losses of the complete solar car system. So, the cost function of the motor model will combine the previously determined operating conditions and the different losses defined in chapter 2.

First, not all losses are influenced by a change in design parameters considered in this study. Although the aerodynamic losses contribute significantly to the total losses in the system, they will change minimally with the design parameters of the motor. So, they are not included in the cost function. Similarly, the bearing losses will also not be calculated. This gives a cost function of $P_{loss} = P_{eddy} + P_{res} + P_{weight}$.

As explained before, the resistance losses will be calculated using the torque profile of the car. The eddy current losses can be found by taking the average angular velocity, while the litz wire data give the mass and resistance values. This results in the following cost function, dependent on the design parameters:

$$P_{loss} = \frac{\pi}{128} \sigma_{copper} \left(\omega_{max} \cdot n_{pp}\right)^2 B_{peak}^2 d_{se}^4 \cdot 3 h_w \cdot 2 n_{pp} \cdot t_m \cdot s_{litz} \frac{1}{\eta_a} + \tag{3.4}$$

$$mean\left(\left(\frac{1}{\sqrt{2}} \frac{\mathcal{T}_r(x)}{K_\tau}\right)^2 \cdot 3 \cdot R_{litz}(s_{litz}, d_{se}, t_m) \cdot \left(1 + \alpha_{copper}\left(T_{motor} - T_{20^\circ}\right)\right)\right) + \tag{3.5}$$

$$x_w \cdot m_{litz}(s_{litz}, d_{se}, t_m) \tag{3.6}$$

This cost function is used to determine the optimal motor design. As an illustration, an example of the output of the model is shown in figure 3.5. Different motor designs with a given P_{loss} for different inputs are shown. Since the magnetic field is currently unknown, a reasonable value was used based on the known motor constants of previous motors and on [26].

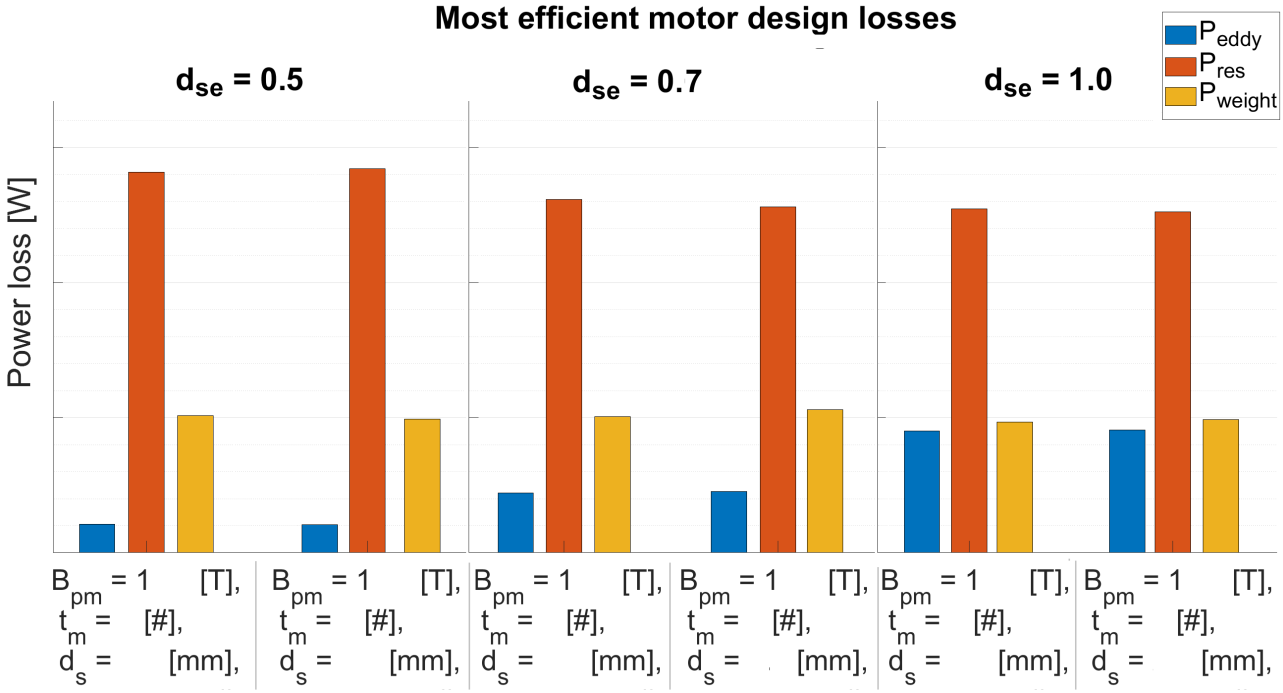

Figure 3.5: Bar plots showing the different P_{loss} values for 2 motor designs for different wire diameters (d_{se}). The designs with the lowest P_{loss} from the model were chosen for each wire diameter. The total P_{loss} is shown above each configuration, and the different motor parameters are shown below the bar plot, where B_{pm} is the magnetic field value, t_m the number of wire turns and d_s the shim distance.

3.6 Conclusion

The chapter described the design parameters of the motor that are considered in this study ans are summarized in table 3.1. They consist of the litz wire specifications and the factors determining the magnetic field strength at the wires. The range in which these can be varied is dictated by the available materials and by the space both inside and outside the motor. Typical operating conditions were presented in the form of a torque profile, this serves as a basis for more detailed resistance loss calculations. The requirements linked to the system current and voltage limits are summarized in equation 3.3. Lastly, the performance of the motor was described by a cost function incorporating resistance, eddy current and weight losses.

These elements are combined in a newly constructed optimization model, which can determine the ideal motor design for the described inputs. The magnetic field is currently not known and must first be mapped to illustrate the function of the model. This experiment is the topic of the next chapter, while the obtained results from the model will be presented in section 5.2 discussed in section 6.1.

Chapter 4

Experiment

In section 2.2.3 the magnetic field in the motor was discussed and in the previous chapter I found the impact of the magnetic field on the motor by analyzing the constructed optimization model. To use the model, more information on the magnetic field is required. This chapter will outline the method used to measure the magnetic field.

The first goal of the test is to find the relation between the magnetic field strength B_{tot} and the air gap d_a, as presented in equation 2.3. The second is to identify the harmonic distortions and the resulting torque ripple relative to the air gap distance, given as $g_{x=d_a}$ in the equation. In section 4.1 the test setup is explained while section 4.2 will focus on the test procedure. The results are presented in the next chapter.

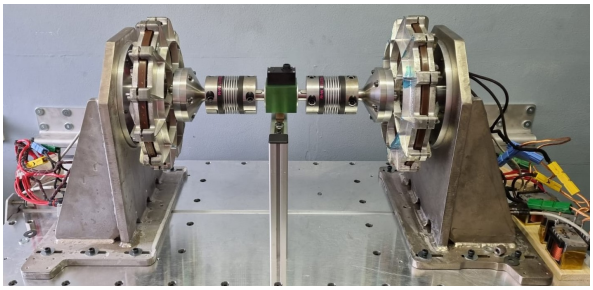

Figure 4.1: The figure shows the Motor Test Bench with two motors mounted and the sensor placed between (green). The motors are connected to the inductors and controller at the back of the two mounting stands.

4.1 Test setup

To measure the magnetic field between the two rings, the induced EMF over a single wire perfectly parallel to the field can be measured. Driving the rotor at a constant speed will result in a given electric angular velocity ω_e, from which the generated waveform can be measured by an oscilloscope. From the measured waveform the magnetic field and harmonic distortion can be found.

The rotor will be rotated in the Motor Test Bench (MTB), a test frame in which two motors can be mounted opposite each other. The motors are coupled with a torque and angular velocity sensor placed in between. The two motors are connected to inductors and driven with two motor controllers, typically connected to a single battery. An image of the MTB is shown in figure 4.1. During the

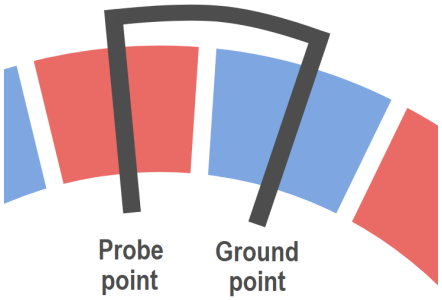

(a) This figure shows placing of the wires relative to the poles.

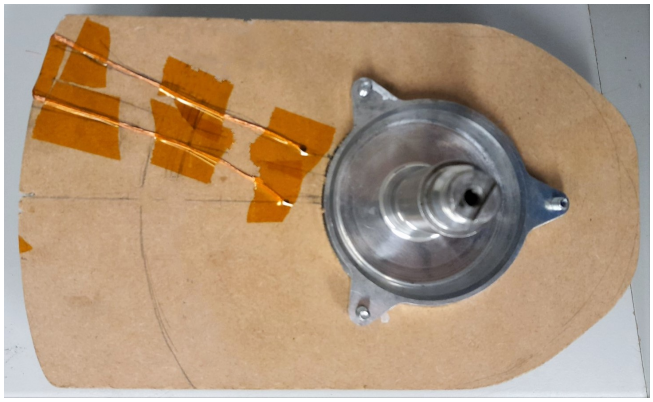

(b) A picture of the wooden construction and wires attached to the shaft used during the experiments.

Figure 4.2: The two figures above show a schematic image and a picture of the wire used to measure the magnetic field.

measurement, a similar setup was used, however no stator was placed in the right motor and the left motor was used to provide a constant angular rotation.

In the right motor, instead of the stator a wooden construction with a wire is attached to the motor shaft. The wire used is a litz wire, which is very thin, such that the wire area is determined only by the angular velocity and the length of the wire inside the field. It was soldered at two ends and placed centered within a single pole and back in another. The test points of the oscilloscope probe are attached to the two ends. This setup is shown in figure 4.2.

The velocity of the rotor was measured by the motor controller and confirmed with the MTB angular velocity sensor. The oscilloscope measured the voltage over a $240ms$ window, with a sampling period of $20\mu s$. This choice was based on limitations of the oscilloscope and the planned measurements speeds. The temperature during the test would have been between 20 and 23 degrees, and will have increased slightly following each test.

The wire measures a single pole during a singe electric period and all pole pairs in a single rotation of the motor. The main problem with the setup is the fact that the poles cannot be identified during rotation. Furthermore, the poles cannot all be measured in a single measurement window of the oscilloscope with the desired sampling period. So, the difference between the pole pairs was separately checked before the measurements and found to be smaller than the accuracy range of the oscilloscope. Therefore, the difference between the poles is assumed to be negligible.

4.2 Test procedure

The measurements were performed at different air gap lengths, with d_s varying in steps of $1mm$. The wire is placed in the center of the magnets each time. To ensure possible vibrations can be isolated from the measurement, the test was performed at different speeds: $200, 400$ and $600rpm$. These vibrations can originate from the MTB, the uneven weight distribution of the rotor and possible disturbances from the PID controller in the inverter. Each set point was measured 3 times to ensure sufficient measurement points for each magnetic pole and to allow for additional verification if required. An example of a measurement result is shown in figure 4.3.

These measurements were completely performed for grade a magnet rings, but not for the lower grade magnet rings. For the grade b and c rings, the measurements were only performed at two

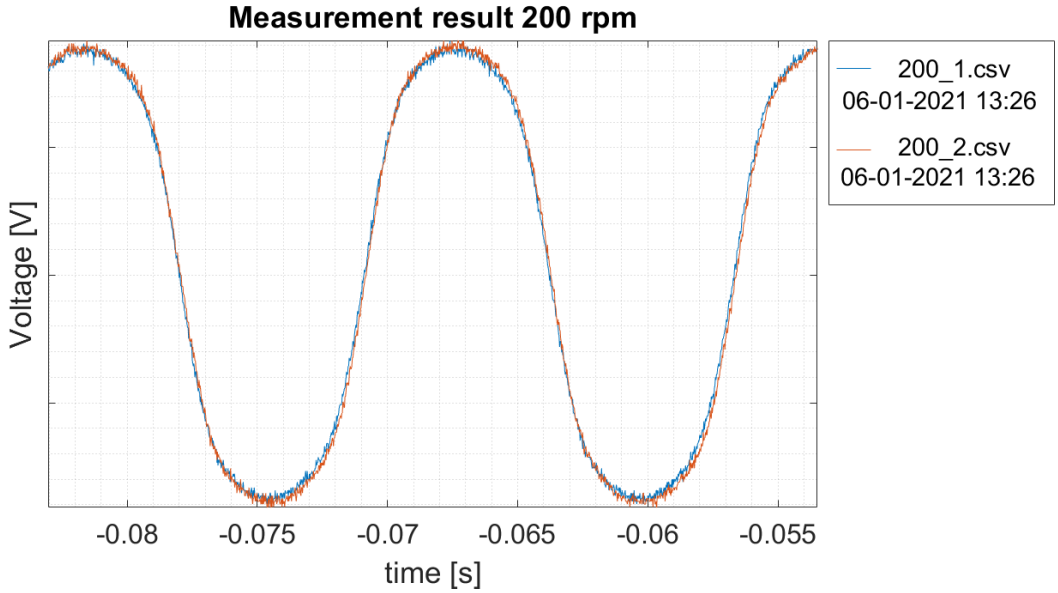

Figure 4.3: In the graph a part of two measurements is shown, measured at $200rpm$*. The axis shows the voltage over the antenna corrected for the angular velocity and length of the wire.*

distances.

4.3 Conclusion

In this chapter the experiment for the measurement of the magnetic field of the STT motor was explained and the test setup was shown. In summary, an antenna is used to measure the field strength and distortions. This test was repeated for different air gap distances and analyzed in the following chapter.

Chapter 5

Results

This chapter will present the results from the experiments described in the previous chapter and the output of the optimization model. Section 5.1 will focus on the measurement results and the description of the magnetic field. This section will conclude by giving the relation between the air gap and the field strength as well as the harmonic distortions found in the experiments.

Using this relation as input for the model, section 5.2 will present the model output. The section will first focus on the motor performance for the given design parameter range. Furthermore, the adherence of any motor design to the requirements is important, so both the total power loss and motor constant K_E are investigated. Next the influence of small changes to the design parameters on the model output is analyzed to find the accuracy of the model. The results presented in this chapter will be discussed in the next chapter.

5.1 Magnetic field measurement results

The data from the experiments is similar to the results shown in figure 4.3, but with different frequencies and amplitudes. This data was analyzed in two steps. First, the discrete Fourier transform is computed for the different measurements. Figure 5.2 shows the complete spectrum of all measurements. The y-axis is zoomed in, showing the amplitude disturbances in the lower regions more clearly. This graph shows that the signal and higher harmonics are present at lower frequencies. However, a small peak is found around $10kHz$ for each measurement. This peak is considered to have resulted from the switching frequency of the motor controller, since it is independent of the angular velocity.

Figure 5.1 shows the relevant part of the frequency spectrum for every angular velocity of the grade a magnet rings. The first and highest peak is at the expected electric angular velocity. When corrected for velocity by plotting the spatial frequency of the Halbach array, the graphs overlap. The next peaks in the spectrum show higher order harmonics at the third and fifth harmonic of the spatial frequency of the array.

In the graphs you can also see that the amplitude decreases with increasing air gap distance. This is more clearly shown in figure 5.3, where the amplitude at different air gap distances corrected for the spatial frequency are given. A margin of $5Hz$ was used around the theoretical spatial frequency peak to calculate the amplitude. Now we can see that the different harmonics decrease exponentially, so an exponential fit using $a \cdot e^{b \cdot d_a}$ can be made. The results are given by the following equations.

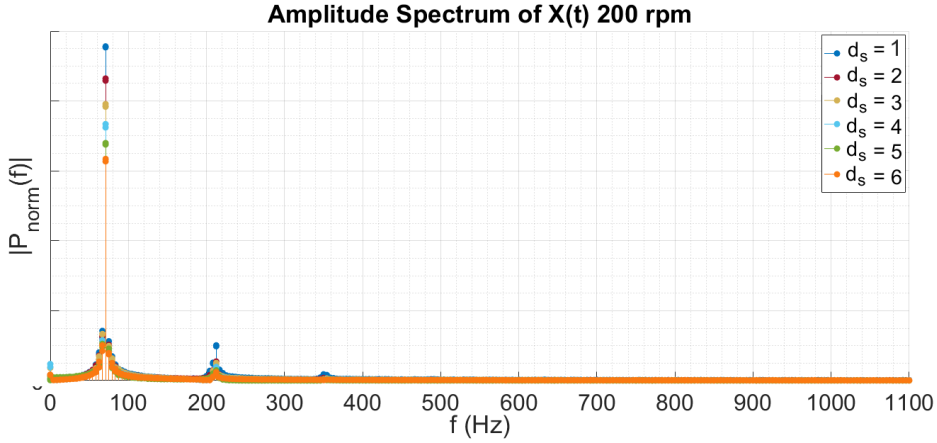

(a) This graph shows the frequency spectrum of the different measurements at $200rpm$. The identified peaks are at $70Hz$, $212Hz$ and $350Hz$.

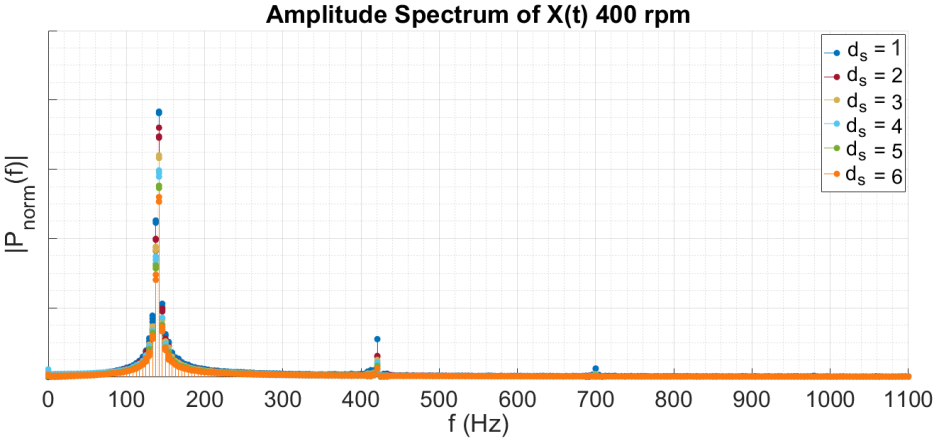

(b) This graph shows the frequency spectrum of the different measurements at $400rpm$. The identified peaks are at $141Hz$, $421Hz$ and $700Hz$. The first peak at $141Hz$ is seemingly significantly lower than the first peak of the measurements at $200rpm$, however note the width of this peak.

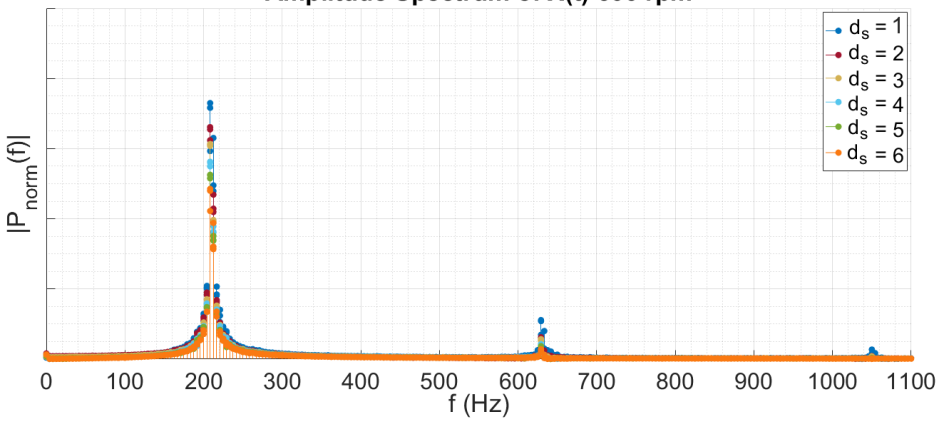

(c) This graph shows the frequency spectrum of the different measurements at $600rpm$. The identified peaks are at $210Hz$, $629Hz$ and $1050Hz$. The first peak at $210Hz$ is seemingly significantly lower than the first peak of the measurements at $200rpm$, however note the width of this peak.

Figure 5.1: These figures show 3 graphs of the grade a magnet ring measurements of different angular velocity in the frequency domain for different shim distances d_s, which give different air gaps. The y-axis shows the amplitude of the different frequencies. This value is based on the voltage measurement corrected for the angular velocity and wire length. Only the relevant area in the frequency spectrum is shown, the rest is shown in figure 5.2.

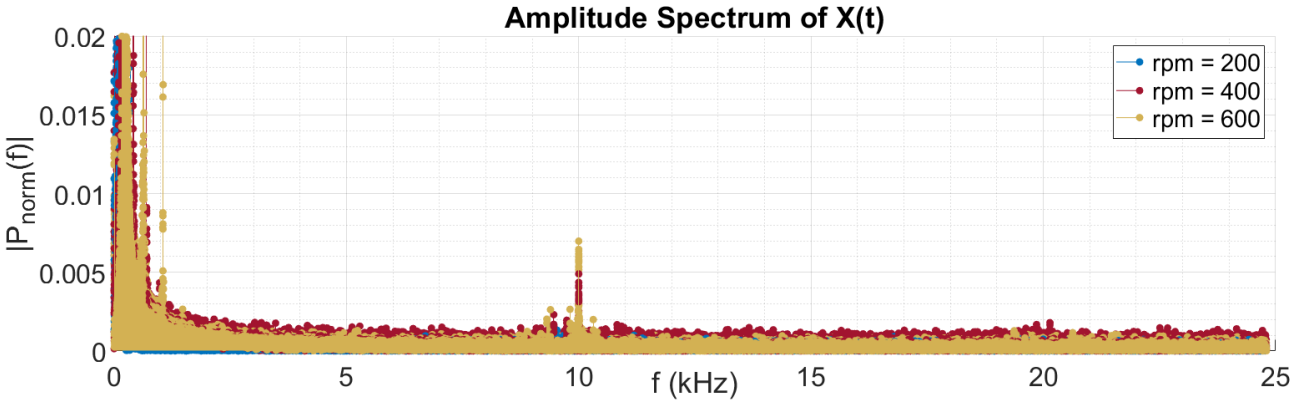

Figure 5.2: This graph shows the results of the different angular velocity measurements in the frequency domain, focused on the higher frequencies which have a lower amplitude. The y-axis shows the amplitude of the different frequencies. This value is based on the voltage measurement corrected for angular velocity and wire length. The peaks shown in the lower frequencies are shown in figure 5.1.

$$B_{h=1} = \square\square\square\square e^{-80.93 \cdot d_a}, \text{ with } CI_a = (\square\square\square\square, \square\square\square\square), CI_b = (-83.41, -78.46) \tag{5.1}$$

$$B_{h=3} = \square\square\square\square e^{-320 \cdot d_a}, \text{ with } CI_a = (\square\square\square\square, \square\square\square\square), CI_b = (-351.5, -289.1) \tag{5.2}$$

$$B_{h=5} = \square\square\square\square e^{-69 \cdot d_a}, \text{ with } CI_a = (\square\square\square\square, \square\square\square\square), CI_b = (-133.9, -4.431) \tag{5.3}$$

Where $B_{h=x}$ represents the peak magnetic field of the x^{th} harmonic of the spatial frequency of the Halbach array. The 95% confidence bounds of the coefficients of the exponential fit $a \cdot e^{b \cdot d_a}$ are given by the CI_a and CI_b.

These fits is consistent with the theoretical analysis of section 2.2.4. The magnetic field of the dual Halbach array configuration can be described with equation 2.3. Using the previous fit results we find:

$$B_{tot}(\theta_e) = \left(\square\square\square\square \cdot 2e^{-0.5 \cdot 162 \cdot d_a} - \square\square\square\square e^{-320 \cdot d_a} - \square\square\square\square e^{-69 \cdot d_a}\right) sin(\theta_e) \tag{5.4}$$

This would mean the peak magnetic field strength at the surface of the Halbach array is $1.048T$. The higher harmonics are subtracted as the resulting peak of magnetic field would be lowered and the torque ripple does not contribute to the torque generation of the motor. In the model this function is simplified by making a fit from the first harmonic, from which the higher order harmonics are subtracted. This is the given by equation 5.5 and would be equivalent to the previous function.

$$B_{tot}(\theta_e) = \square\square\square\square e^{-65 \cdot d_a} sin(\theta_e) \tag{5.5}$$

Finally, the measurements of the lower grade magnet rings were analyzed and found to result in a similar frequency domain plot, though with less data. A fit of the magnetic field strength was made using the found relation above, but corrected for the lower grade magnet rings. This results in a peak magnetic field strength B_{tot} function of $\square\square\square\square e^{-65 \cdot d_a}$ for grade b and $\square\square\square\square e^{-65 \cdot d_a}$ for grade c magnets. In the next section these functions will be used as input for the model.

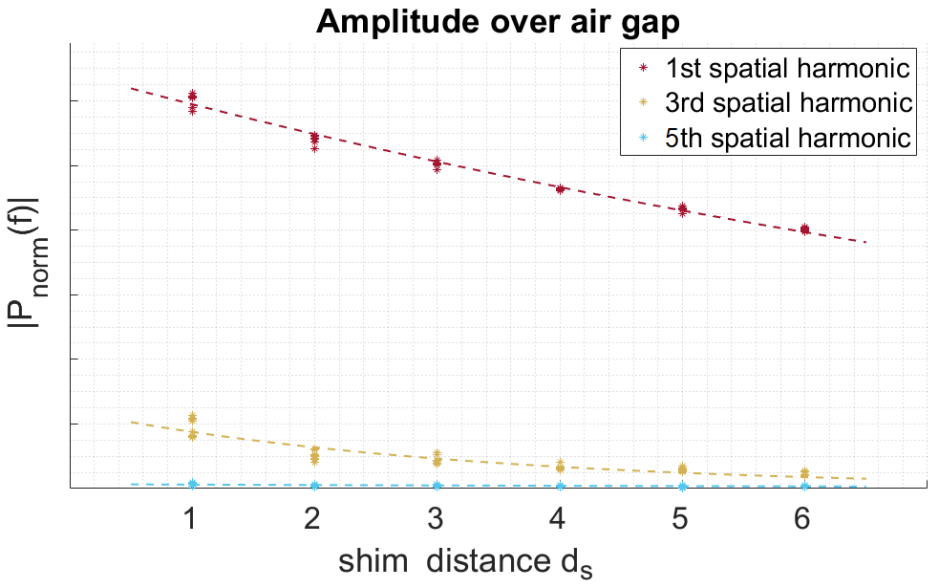

Figure 5.3: The graph shows the relation between amplitude degradation and an increase in air gap. The 3 different harmonics are plotted and the fit of each is shown. The amplitude is corrected for spatial frequency and angular velocity of the different measurements

5.2 Model results

In this section the different outputs from the model will be presented, these results are interpreted and discussed in the following chapter. Since the performance of the motor is a focus point of this research, the total losses and motor constants for different motor designs will be presented first. Next the influence on the performance of the design parameters and uncertainties of the model will be analysed using their estimated variation.

The data used in the analysis is presented in the table below. The range within the parameters considered in this study can be varied is based on section 3.3. The variation in B_{pm} is based on the calculated confidence interval of the magnetic field measurements, while the wire layout parameters are estimated based on the manufactures data sheet [24] and previously constructed motors. The variation of the diameter of the litz wires d_{se} is given as a percentage of the cross sectional area of the wires. Moreover, the variation in the number of litz strands s_{litz} was changed for each litz strand diameter, because it is assumed thicker strands are less likely to be damaged.

Table 5.1: Overview model inputs used

Parameter	***Range***	***Variation***
t_m	□ - □ [#]	-
d_s	□□ - □□ [mm]	0.01 [mm]
B_{pm}	□□□□, □□□□, □□□□ [T]	0.05 [T]
d_{se}	□□□,□□□, □□□ [mm]	0.1% $\cdot A_{se}$
s_{litz}	-	20, 10, 5 [#]
η_a	□□□	0.05
η_c	□□□	0.02

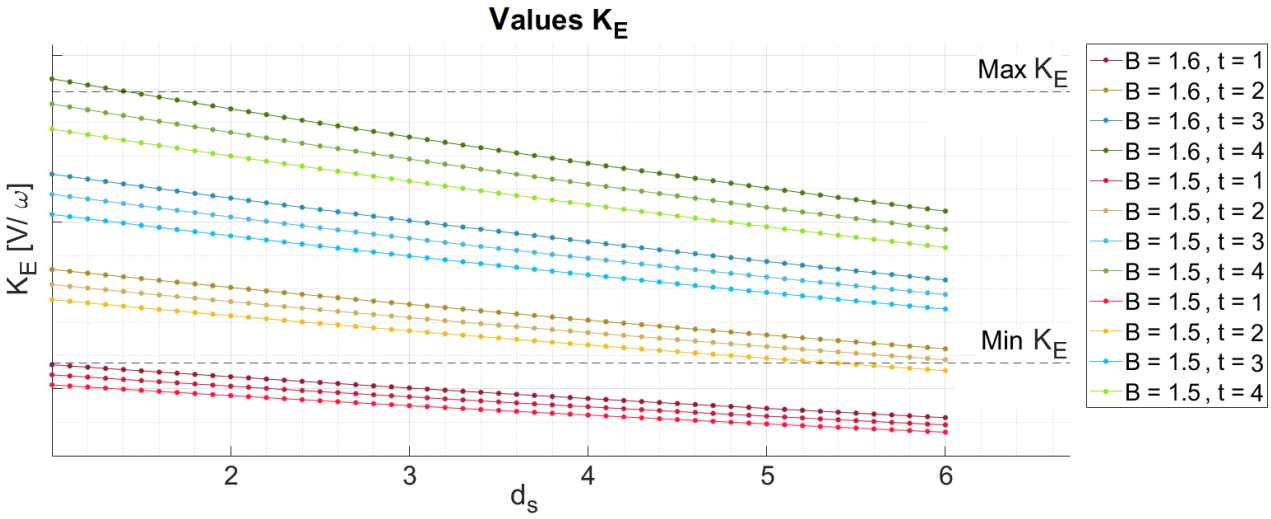

Figure 5.4: The graph shows the back-EMF motor constant K_E value for different optimized test motor designs, which have different magnet grades B_{pm} and number of turns t_m. K_E is plotted against the air gap d_a represented in the related shim distance d_s. The different magnetic grade values are shown in different colors, however they may look similar in the image, know that a higher B_{pm} value will result in a higher the motor constant value.

5.2.1 Model output

An example of the output of the model was already shown in figure 3.5, which shows the different losses of the cost function for optimized motor designs in a bar chart. In the graphs of figure 5.5 the total loss for all possible combinations of parameters within the range is presented. These results have not been filtered to meet the requirements. Furthermore, the number of litz wire strands s_{litz} is not shown in this figure, but this parameter was optimized following the model work flow from section 3.1.

The back-EMF motor constant K_E data is shown in figure 5.4, relative to the the air gap d_a. An example of the requirement given in equation 3.3 is added to the graph. When the model is used, all K_E values that fall outside the maximum and minimum are invalidated. The limits on the design parameters have been used to determine the ranges, so the motor designs only need to be filtered for a valid motor constant to determine if it can be used.

5.2.2 Model parameters analysis

In this section the influence of the different design parameters and uncertainties is presented for both the total loss P_{loss} and the motor constant K_E. The relative influence was calculated using the determined expected variation of each parameter in the table for each data point in the range. From this data the mean and the standard deviation were calculated. This is plotted in figures 5.6a and 5.6b. Not all parameters are plotted for the motor constant graph, as changes in these parameters do not influence the constant.

To determine the significance of a parameter's influence on the performance, a set margin was established for the losses and motor constant. The P_{loss} boundary was based on the differences between similar motor designs given in the model output and what would be an acceptable loss accuracy for Solar Team Twente. The motor constant boundary was calculated for an $1[V]$ difference at the maximum speed. This has resulted in $\pm 0.5[W]$ and $\pm 9.3[mV/\omega]$ respectively.

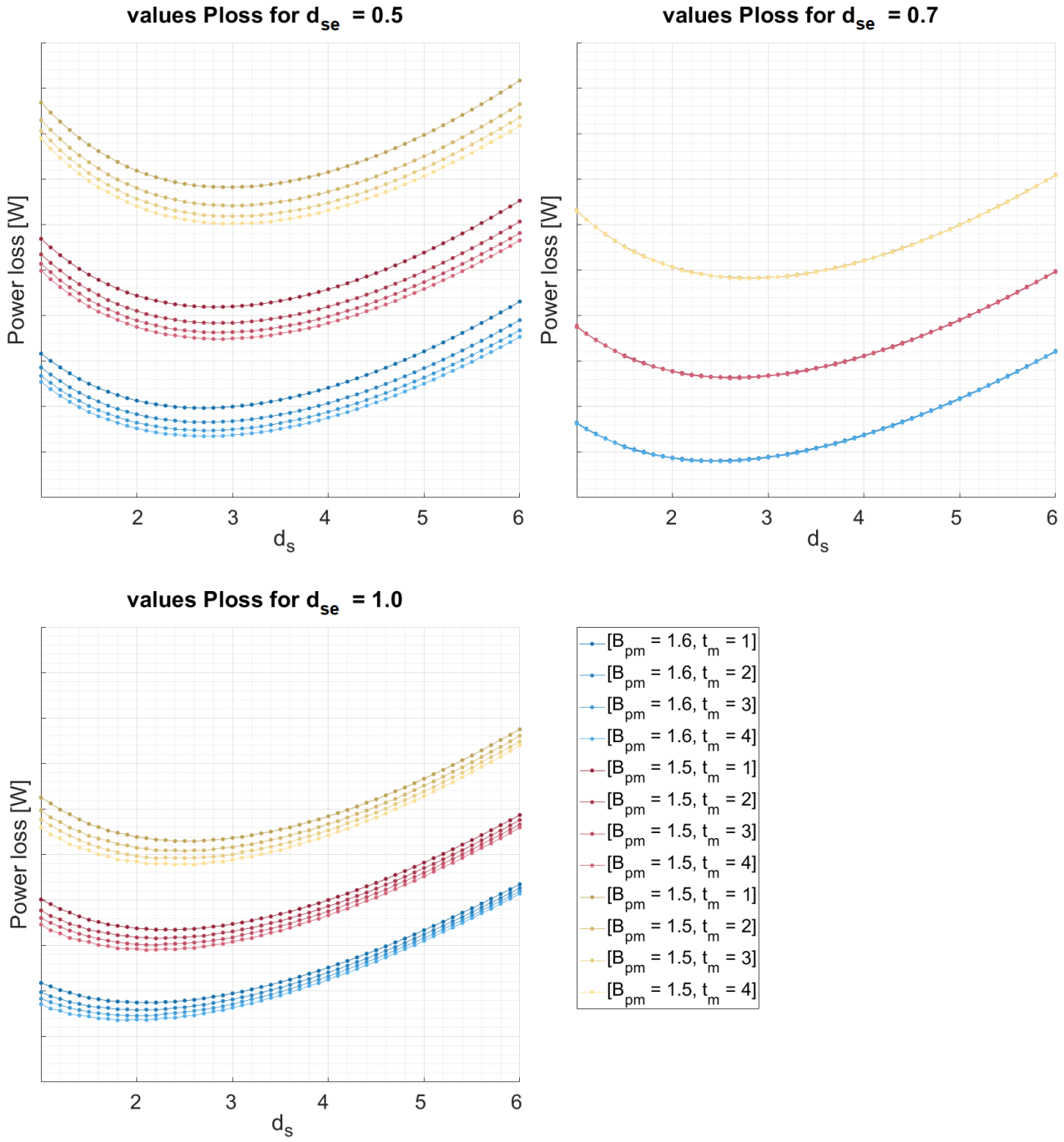

Figure 5.5: The total loss P_{loss} of different optimized test motor designs. The test motor designs are varied for the given range of design parameters. The total loss is plotted against the air gap d_a represented in the related shim distance d_s. The different magnet grades B_{pm} and litz wire diameters d_{se} are clearly distinguished. The different number of wire turns t_m is also shown, however the total losses are very similar and even almost overlap for $d_{se} = 0.7$.

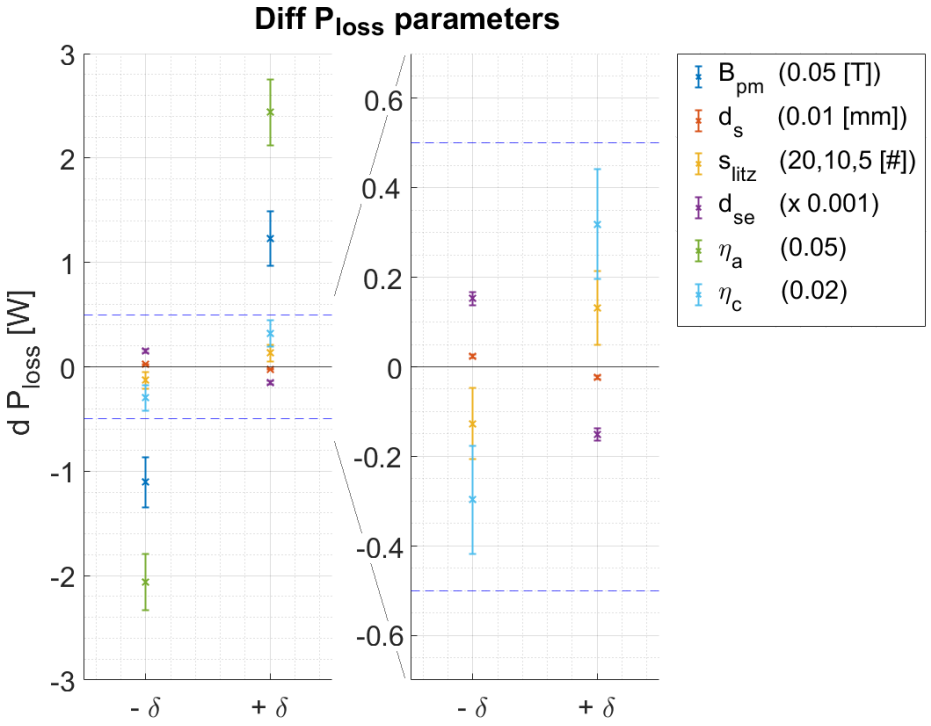

(a) Errorbar chart of the design parameters and uncertainties influence on the total loss P_{loss}. A zoomed in version in added on the right for clarity.

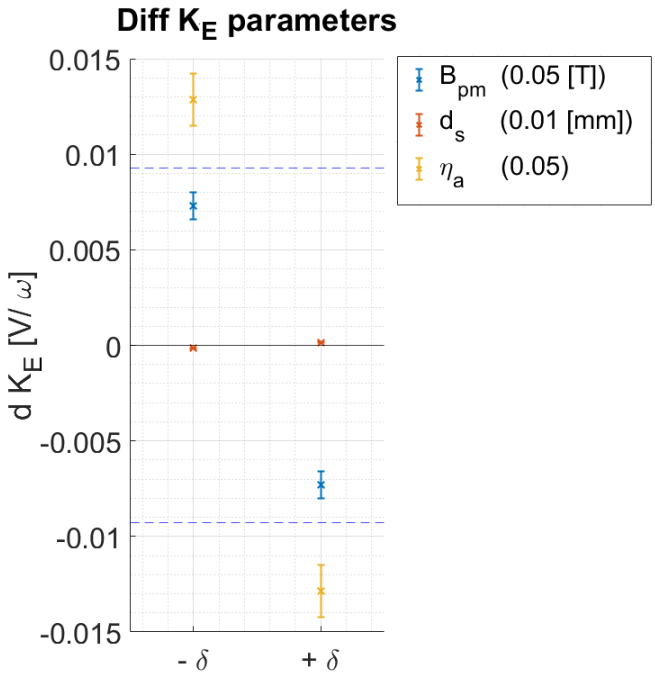

(b) Errorbar chart of the design parameters and uncertainties influence on the motor constant K_E, normalized for the number of turns.

Figure 5.6: These figures show the influence of the offset on the performance of the motor. The influence of variation in the parameters is shown with an 'x' as the mean of the deviation and the bars representing the variance of the deviation (based on the standard deviation). The blue dotted line represent the line where above the parameter has a significant influence on the losses.

5.3 Conclusion

In this chapter the relation between the magnetic field and air gap was found. Furthermore, the higher harmonics present in the magnetic field were discovered and linked to the air gap. These results can be summarized by equation 5.4. Using this function for the magnetic field, the output of the model was determined for the range in which the design parameters can be varied. The results are presented in figures 5.5 and 5.4. Lastly, the influence on the performance of the design parameters and uncertainties was analyzed using their expected variation. This is presented in figure 5.6.

Chapter 6

Discussion

This chapter will discuss the implications and limitations of the model as well as the interpretation of the results of the magnetic field experiment and the model output presented in the previous chapter. First, section 6.1 will review the model. This section is further divided into the subsection 6.1.1, which interprets the model output and identifies interesting observations, and subsection 6.1.2, which discusses the analysis of the model parameters and their influence on the performance. Section 6.2 will evaluate the experiment and its results. The last two sections focus on the verification of the model with existing data and the implications of this comparison.

6.1 Model

The model presented in this thesis has optimized the STT motor design for the key design parameters: the windings configuration and the air gap. Furthermore, it has given insight into the losses of the motor within the system for different mechanical and electrical requirements, limits and operating conditions. If wire and magnetic field data is provided, it should be able to optimize any 3-phase coreless axial flux permanent magnet (AFPM) motor for a specific application. But it is important to clearly define the operating conditions of the application. For example, average driver behavior data can be used to optimize an electric vehicle motor to ensure the correct output. Moreover, I would recommend looking at the 10 best motor designs when using the model. From these options the user should evaluate which design can be most successfully produced.

This evaluation can be based on graphs like figure 3.2, which could be generated for each design. These graphs show the influence of using less litz wire strands more clearly. If the influence is minimal, a smaller value of s_{litz} could be chosen. This would ensure the wires will more easily fit inside available space in the stator and the magnet rings are less likely to scrape against the stator. If small changes in the number of strands result in significant losses, another motor design with initially higher losses could be preferred to allow for more error during production. Similarly, the number of turns in the motor can impact the production and should be taken into consideration when evaluating the designs. Depending on the assembly of the wires in the stator, an even number of turns could result in better alignment.

However, if the optimization problem becomes larger the run time of the code might be a problem. The model is currently constructed to loop through every possible motor design, which is not ideal. There are several options to improve the calculation speed, like invalidating motor designs when the motor constant has been calculated before optimizing the wire layout. It is also possible to define a smaller region of interest by using the found relations between parameters and reviewing the output of the model. Lastly, step sizes of the model are currently relatively small to get the required accuracy,

but can be increased if the accuracy loss is not a problem. I recommend looking into these options if the run time of the model becomes a problem.

6.1.1 Interpretation results

This subsection will focus on the results from the model given in section 5.2. The goal is to identify interesting correlations or patterns. The different observations and their implications are summarized below.

Magnetic field strength The graphs from figure 5.5 show that higher magnetic fields, where B_{pm} is larger, are more optimal. Looking at the trend, it might be valuable for STT to develop an array with greater strength even if this would add more weight to the motor.

Ideal air gap The curves from figure 5.5 also show that an ideal air gap is present depending on the magnetic field strength. This distance tends to be greater for smaller strand diameters d_{se} and lower magnetic fields. This is expected, since a lower magnetic field implies a lower torque constant and therefore more current. Smaller strand diameters will have relatively more resistance per area of of the total bundle. A greater distance would allow for more strands and decrease the ohmic power losses. However, the fact that such a clear ideal air gap can be seen in the graphs was an unexpected result. This greatly simplifies the design process if the system requirements are easily met.

Optimal litz strand diameter The most optimal litz strand diameter d_{se} depends on the magnetic field, as larger diameters perform better at lower magnetic fields, while the opposite is true for smaller litz wires. This could be explained by the increased eddy current losses at higher magnetic fields. It implies that the range of litz strand diameters should be selected depending on the magnetic field strength range.

Number of turns Looking back at figure 5.5, it can be concluded that the number of turns in the motor have relatively little influence on the total losses. The fact that the number of turns does not have a significant influence on the losses was unexpected, since it determines the motor constant in large part. This relation can also be seen in figure 5.4. However, this would imply that limiting the motor constant will not have a significant influence on the performance of the motor. This is only true if the current and voltage of the system allow for a large enough valid range, given by equation 3.3.

Figure 5.4 also shows that designs with fewer turns result in a smaller range of K_E values covered by the designs (i.e. the value of K_E for the same number of turns varies less by changing the air gap or magnetic field). This implies that the only valid design could have large losses if the maximum limit of K_E decreases. The reason is that a stator with a single turn cannot easily be made with the current production process. So, a lower magnetic field must be used which increases the motor losses significantly. Therefore, systems that require a low motor constant will benefit from a different, smaller motor geometry.

6.1.2 Model parameters analysis

The influence of the different design parameters as presented in subsection 5.2.2 is discussed below. The parameters are closely linked and their influence on the performance will strongly depend on the analyzed region. The analysis of the parameters was based on the range and variations given in table 5.1. The data from the analysis is shown in figure 5.6. We can see that the alignment factor η_a and the magnetic field strength B_{pm} cause significant changes to the total losses, so I will focus on these parameters.

Alignment factor The alignment factor has significant influence on both the motor constant K_E value and the losses. This can easily be explained as it directly impacts the motor constant, lowering it at a higher misalignment, which causes an increase in ohmic power losses for the same weight losses. The main problem with the alignment variation in the motor constant K_E is that a realized motor might not meet the requirements of equation 3.3, rendering it useless. Improving the alignment variance is important to create a robust and accurate model and this will be further discussed in section 6.4.

Magnetic field The magnetic field variance mainly influences the total losses, which means a realized motor might have more losses than expected. However, the magnetic field value would not actually vary, as it is an inherent characteristic of the arrays. The variance was based on the 95% confidence interval of the measurements. So, the accuracy of the measurement was not sufficient to run the model within the ideal P_{loss} boundary. The experiment and possible improvements will be discussed in the next section.

6.2 Magnetic field experiment

The data from the measurements was successfully used to determine the magnetic field for different air gaps and matched the expected function, which resulted in equation 5.5. This result is supported by the fact that the generated amplitude for the different velocities match when corrected for spatial frequency. However, the data was not accurate enough, as already talked about in subsection 6.1.2. The confidence interval from the fit gave a expected total magnetic field B_{tot} variance of $0.0387T$ on average within the analyzed region. This resulted in a lower accuracy of the model.

This high interval could have been prevented in part by a higher number of measurements. The current measurements seem sufficient for the 1st spatial harmonic, however the higher harmonics show more deviations. These deviations can be seen from the 95% confidence bounds in equations 5.2 and 5.3. More measurements at different shim distances would have reduced the error, specifically for higher harmonics.

Another problem that was identified after the measurements is the accuracy of the voltage measurements. The data from the oscilloscope had an error margin of about 0.5% due to the record settings while reading out the acquisition memory, the set sampling rate and the signal repeat. This accuracy could be increased by using an oscilloscope with higher specifications, but also by measuring at lower velocities. Lower angular velocities would allow for a larger difference between the sampling frequency and electric frequency, giving a more accurate amplitude spectrum. This is already demonstrated by the differences between the frequency domain graphs of $200rpm$ and $400rpm$.

It is also possible to construct a simulation of the specific Halbach array, which could be used in cooperation with the experimental results to find the desired accuracy. However, I am not sure if the desired accuracy can be reached with a simulation. The effects of non-ideal factors, such as inhomogeneity of the magnets or manufacturing tolerances, would be ignored. So, I would recommend STT to repeat the measurements using the above improvements to ensure the desired accuracy of the model.

Since this thesis is written after the actual research, I know this was not done by the team. Instead, magnetic flux measurements from produced motors were compared to the model data. The calculated magnetic field from these flux values was found to be slightly (2%) higher than determined in this research, which falls within the confidence bounds. Now this new, slightly higher, value has been used in the model.

6.3 Model Verification

Since the model was made to optimize only the parameters that can be readily varied in the current motor, it is possible to verify the model with data from past motors. However, the total loss calculation and producibility of the model are more difficult to verify completely for a produced motor. So, different elements of the model are verified separately and it is assumed that the model is working as intended if individual elements are correct.

The cost equation of the model includes the weight, resistive and eddy current losses. These different equations have already been verified by STT or myself in section 2.2. I found that the losses in the motor are accurately described, but the eddy current losses have only been checked for a single motor design. Ideally, the losses would be measured for more winding layouts to ensure they are calculated correctly.

Similarly, the different assumptions that were made to ensure a producible motor design were based on previously produced motor. This includes the values used for the compression and alignment factor, but also the required air gap margins and windings variations. Based on the data from STT, there have been no problems in the motor production when adhering to these values, so they are considered valid.

The motor constants equations 2.15 and 2.23 could not be verified, since the relation was determined in this research and the magnetic field was unknown. Using magnetic flux, shim distance and wire turns data courtesy of STT, this relation can be verified. The magnetic flux data was determined by measuring the voltage difference over the windings when the motor is rotating, assuming no-load this would be the back-EMF of the motor. This data was normalized for the number of wire turns.

The measurements and model output is shown in figure 6.1. The graph shows that the calculated flux values are comparable to the measured flux points and that they follow the general trend of the calculated data. However there are large differences between the measured flux data points.

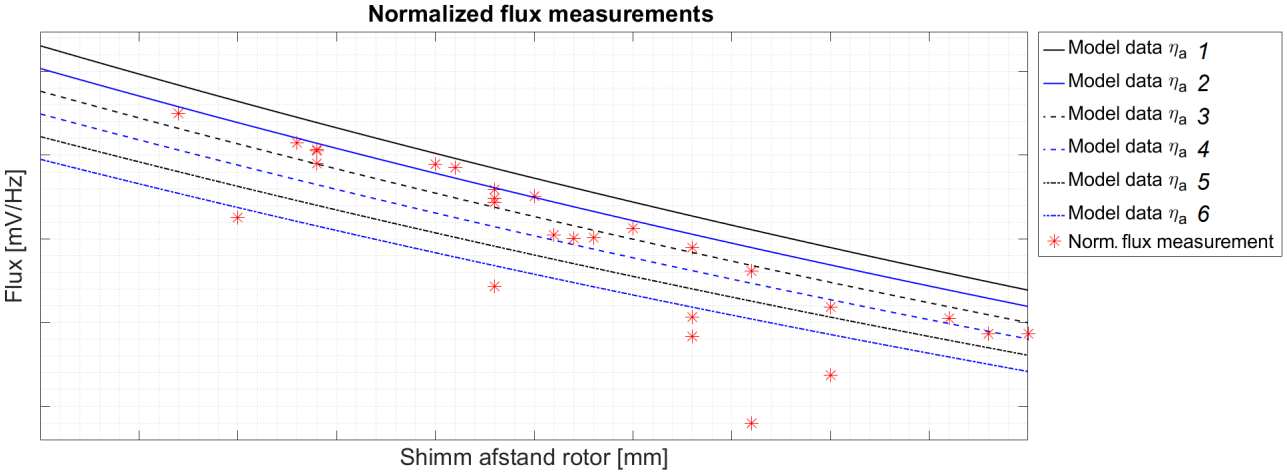

Figure 6.1: The different magnetic flux values of produced motors are shown, normalized for the magnetic field strength and wire turns. The lines show the model output of the magnetic flux, based on the motor constant equation of K_E, equation 2.23.

The alignment factor was assumed to be □□, but even the expected variation in alignment (0.05) does not explain the large spread in flux measurements. It could be explained by differences between the magnetic rings used in these measurements, but figure 5.6b shows that these difference should be large to justify the spread. Although it is possible for the magnets to demagnetize, STT generally manufactures a new ring (or remakes an old ring because of mechanical errors) each edition. No

significant differences have been observed between older and newer magnet rings. This means that the assumptions made about the alignment factor were incorrect and it varies more than expected.

6.4 Alignment factor

If this was a normal thesis, I would recommend to investigate the alignment of the wires in more detail. Furthermore, the production process should be improved for better wire alignment, which would also allow you to check if no other parameter influences the motor constant measurements. However, this paper is written after the research was concluded and actions have already been taken to verify the influence of this factor. The results will be presented here shortly.

To check the alignment of the wire after a stator is produced X-ray images were taken to be able to see the wire position. An edited image of these X-ray images is shown in figure 6.2. Similar images confirmed that the low and high values of the magnetic flux for similar distances, shown in figure 6.1, were mostly the result of misalignment. A small part of this variation is expected to be the result of a non-centered stator in a magnetic field.

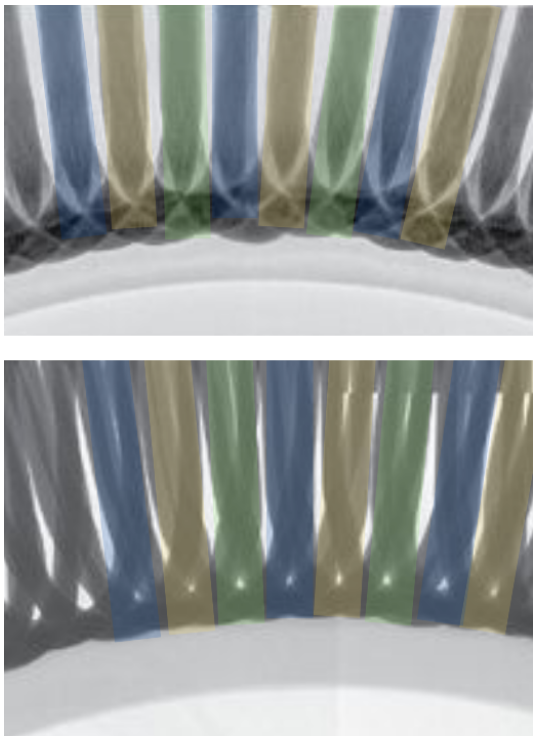

Figure 6.2: This image shows two X-ray images of the stator wires. An overlay was added to show the position of the wires of the different phases. The stator above shows a very orderly layout of the wires and has little misalignment, however the stator below shows that the wires moved from the position during production.

Using these images a more clear distinction could be made between what are considered 'good' and 'bad' stators. It remains difficult to quantize the misalignment, but certain 'alignment bins' have been established. Furthermore, a factor above □□ can now be ensured by the current improvements to the production method and some choices made during this process. This improvement was a direct result of creating more focus on aligning the wires as well as the increased insight in the wire position after potting. There is still room for improvement and several options are currently being considered by the team.

Unfortunately, after this research was finished and the model could be used more reliably, the team was presented with a new challenge for the motor: a different race with hills. These hills result in higher currents in the motor for a longer amount of time, which produce heat and would eventually melt the motor. So, the focus was shifted to investigate this new problem and later to implement water cooling into the motor. The research used in this paper was helpful to realize this more efficiently and quickly, however the model was not used to design the final motor of the solar car. Possible improvements and errors will likely still be found in the following edition.

6.5 Conclusion

This chapter discussed the main limitations and errors in the model. It also identified interesting observations, such as the presence of an ideal air gap in this motor design or the fact that the turns in the motor do not have much influence on the losses. The current error in the model is considered too high and to increase the accuracy of the model, the magnetic field experiment should be repeated at lower speeds with more air gap data points.

Lastly, the chapter focused on the verification of the model and the alignment factor. The data from realized motors differed greatly from the expected range. The reason was assumed to be incorrect assumptions about the value of the alignment factor and its variation. This was confirmed by follow-up research described in section 6.4.

Chapter 7

Conclusion

In this thesis a model to optimize the performance of a 3-phase coreless brushless axial flux permanent magnet machine with dual Halbach arrays is presented. The impact of small changes in the windings configuration and the air gap on the motor efficiency is described by this optimization model.

First, this specific motor was described and the relevant relations between the layout and losses were found. Next, the key design parameters and performance were identified and used to construct the model. Since the magnetic field was not known, an experiment was performed that gave the relation between the total magnetic field strength of the dual Halbach arrays and their air gap. With this relation, the influence of the key design parameters was then investigated using the output of the model and their expected variance.

The output of the model showed the presence of an ideal air gap in this motor design. Furthermore, the number of turns in the windings configuration does not have much influence on the total motor losses in an optimized design. However, the confidence interval of the fit of the magnetic field was considered to be too high to guarantee the desired accuracy of the model for Solar Team Twente. Finally, the performance is greatly influenced by the alignment of the wires. Research into producing greater alignment in the motor is required to ensure higher model accuracy and motor performance.

The current model and framework can be used to help optimize 3-phase coreless brushless axial flux PM machine with dual Halbach arrays. This research could also contribute to further development of axial flux motor design models, specifically in the actualization of a motor from model parameters. For Solar Team Twente the research has increased the robustness of the design significantly and improved the production process by more clearly identifying the parameters influencing the performance of the motor. The model been a successful tool to help design an ideal motor for a solar car.

Recommendations

Several recommendations have already been given in the thesis, but the main recommendations are summarized below.

- More research into improving the alignment of wires would help improve the motor. Furthermore, finding a way to quantize this factor for a given motor would reduce the uncertainty of the

model. This might result in the identification of more relevant model input that will increase the robustness of the model and eventually improve the performance of the motor.

- The magnetic field experiments should be repeated at lower angular velocities and with more data points for more different air gaps. This will reduce the error from the experiment and result in a model with a higher accuracy.
- If the requirements for the Solar Team Twente motor change, for example when the race is changed and the load case changes, the model can be expanded. It is recommend that the new design variables would include the motor diameter, number of pole pairs and number of motors used to drive the car. Changes to only these parameters are most likely to meet the new requirements while allowing for an optimal design.
- When the model is used for a larger range, or when it is expanded to use for more parameters, the calculation speed should be improved. There are several options to do this, but it would be recommended to do this based on the new optimization problem. It should be mentioned that the model is currently deliberately not efficient, since this would give a more detailed output and the current execution time is not a problem.
- Research into a complete analytical design models of 3-phase coreless brushless axial flux PM machine with dual Halbach arrays would require an analytical description of Halbach arrays. This description should be able to find the magnetic field of different geometries and optimize the power density for an array. Although research into this type of analysis exists, no complete analytical model could be found that would be applicable to this type of motor. This research will likely be more relevant for weight critical systems.

Chapter 8

Acknowledgments

I would like to thank my supervisors, M. Dhallé and E. de Weerd, for their guidance and suggestions. Thanks to them I was able to write this report how I wished it would be written.

I would like to thank my own and previous team members of STT. They allowed me to make time to do this research during a very busy year and their suggestions and questions often helped me towards the correct answers.

I also wish to thank my friends for their support and patience with me.

Finally, I want to thank my family for their encouragement and advice. I specifically want to thank my mother, I do not think I could have done this if she had not helped me.

Bibliography

[1] F. Giulii Capponi, G. De Donato, and F. Caricchi, "Recent advances in axial-flux permanent-magnet machine technology," *IEEE Transactions on Industry Applications*, vol. 48, no. 6, pp. 2190–2205, 2012.

[2] N. Chayopitak and D. G. Taylor, "Performance assessment of air-core linear permanent-magnet synchronous motors," *IEEE Transactions on Magnetics*, vol. 44, no. 10, pp. 2310–2316, 2008.

[3] N. Taran, V. Rallabandi, G. Heins, and D. M. Ionel, "Coreless and conventional axial flux permanent magnet motors for solar cars," *IEEE Transactions on Industry Applications*, vol. 54, no. 6, pp. 5907–5917, 2018.

[4] B. Cheng, G. Pan, and Z. Mao, "Analytical calculation and optimization of the segmented-stator dual-rotor axial flux permanent magnet motors," *IEEE Transactions on Magnetics*, vol. 56, no. 11, pp. 1–9, 2020.

[5] H. Lovatt, V. Ramsden, and B. Mecrow, "Design of an in-wheel motor for a solar-powered electric vehicle," *Electric Power Applications, IEE Proceedings* -, vol. 145, pp. 402 – 408, 10 1998.

[6] A. Cavagnino, M. Lazzari, F. Profumo, and A. Tenconi, "A comparison between the axial flux and the radial flux structures for pm synchronous motors," *IEEE Transactions on Industry Applications*, vol. 38, no. 6, pp. 1517–1524, 2002.

[7] M. Aydin, M. Gulec, Y. Demir, B. Akyuz, and E. Yolacan, "Design and validation of a 24-pole coreless axial flux permanent magnet motor for a solar powered vehicle," in *Proceedings of 2016 XXII International Conference on Electrical Machines (ICEM)*, 2016, pp. 1493–1498.

[8] K. Duffy, "Optimizing power density and efficiency of a double-halbach permanent-magnet ironless axial flux motor," in *Proceedings of the 52nd AIAA/SAE/ASEE Joint Propulsion Conference*, 07 2016.

[9] T. F. Tallerico, J. C. Chin, and Z. A. Cameron, "Optimization of an air core dual halbach array axial flux rim drive for electric aircraft," in *Proceedings of the 2018 Aviation Technology, Integration, and Operations Conference*, 2018.

[10] F. Sahin, "Design and development of a high-speed axial-flux permanent-magnet machine," Ph.D. dissertation, Technische Universiteit Eindhoven, Electrical Engineering, 2001.

[11] R. Al Zaher, "Axial flux permanent magnet motor csiro: New frame design, analysis, steady state model and comparison to radial flux permanent magnet motor biel," Master's thesis, TU Delft, Delft University of Technology, Mechanical Engineering, Apr 2010. [Online]. Available: https://repository.tudelft.nl/islandora/object/uuid:029674d0-3844-4b92-be6d-90bdcc4b9dad?collection=education

[12] S. Zhou, P. Walker, Y. Tian, C. T. Nguyen, and N. Zhang, “Comparison on energy economy and vibration characteristics of electric and hydraulic in-wheel drive vehicles,” *Energies*, vol. 14, no. 8, 2021. [Online]. Available: https://www.mdpi.com/1996-1073/14/8/2290

[13] C. Wei and H. Taghavifar, “A novel approach to energy harvesting from vehicle suspension system: Half-vehicle model,” *Energy*, vol. 134, pp. 279–288, 2017. [Online]. Available: https://www.sciencedirect.com/science/article/pii/S0360544217310289

[14] K. M. I. . A. L. P. P. 18947, “Halbach arrays.” [Online]. Available: https://www.kjmagnetics.com/blog.asp?p=halbach-arrays

[15] C. Ma, W. Zhao, and L. Qu, “Design optimization of a linear generator with dual halbach array for human motion energy harvesting,” *2015 IEEE International Electric Machines & Drives Conference (IEMDC)*, pp. 703–708, 2015.

[16] D. Månsson, “On the optimization of halbach arrays as energy storage media,” *Progress In Electromagnetics Research*, vol. 62, pp. 277–288, 04 2015.

[17] L. Yan, L. Zhang, J. Yao, H. Hu, C. Chen, and I.-M. Chen, “A tubular linear machine with dual halbach array,” *Engineering Computations*, vol. 31, p. 77, 04 2014.

[18] N. Borchardt and R. Kasper, “Analytical magnetic circuit design optimization of electrical machines with air gap winding using a halbach array,” in *2017 IEEE International Electric Machines and Drives Conference (IEMDC)*, 2017, pp. 1–7.

[19] “Engineering toolbox, (2003). resistivity and conductivity - temperature coefficients common materials.” [Online]. Available: https://www.engineeringtoolbox.com/resistivity-conductivity-d_418.html

[20] X. Nan and C. Sullivan, “Simplified high-accuracy calculation of eddy-current loss in round-wire windings,” in *2004 IEEE 35th Annual Power Electronics Specialists Conference (IEEE Cat. No.04CH37551)*, vol. 2, 2004, pp. 873–879 Vol.2.

[21] P. B. Reddy, T. M. Jahns, and T. Bohn, “Modeling and analysis of proximity losses in high-speed surface permanent magnet machines with concentrated windings,” *2010 IEEE Energy Conversion Congress and Exposition*, pp. 996–1003, 2010.

[22] W. Zhao, X. Wang, S. Wu, S. Cui, C. Gerada, and H. Yan, “Eddy current losses analysis and optimization design of litz-wire windings for air-core compulsators,” *IEEE Transactions on Plasma Science*, vol. 47, no. 5, pp. 2532–2538, 2019.

[23] J. Gieras, R. Wang, and K. M.J., *Axial Flux Permanent Magnet Brushless Machines. Chapter 2: Principles of AFPM Machines, Chapter 5: AFPM Machines Without Stator Cores and Chapter 6: AFPM Machines Without Stator and Rotor Cores*, 2nd ed. Springer, 2008.

[24] R. P. G. . C. KG, “Pack litzwire: Rupalit classic.” [Online]. Available: https://www.packlitzwire.com/products/litz-wires/rupalit-classic/

[25] “bridgestone world solar challenge regulations 20-27 october 2023, release version 1.0, issued 22 april 2022,” May 2022. [Online]. Available: https://worldsolarchallenge.org/media/3tfjojkj/2023-regulations-release-version-1-22042022.pdf

[26] S. Sadeghi and L. Parsa, “Multiobjective design optimization of five-phase halbach array permanent-magnet machine,” *IEEE Transactions on Magnetics*, vol. 47, no. 6, pp. 1658–1666, 2011.